CHARACTERIZATION OF NANOPARTICLE AGGREGATES USING INVERSE FORMULATION AND DISCRETE-DIPOLE APPROXIMATION

by

Ozan Burak Eriçok

B.S., Mechanical Engineering, Boğaziçi University, 2014

Submitted to the Institute for Graduate Studies in
Science and Engineering in partial fulfillment of
the requirements for the degree of
Master of Science

Graduate Program in Mechanical Engineering
Boğaziçi University

2017

ACKNOWLEDGEMENTS

I would like to thank my advisor Prof. Hakan Ertürk for his continuous support of my academic study and research. Without his guidence, I would probably get lost during my research and would never get the opportunity to write this thesis. The advices he has given priceless. I would also like to thank Prof. Ali Taylan Cemgil and Prof. Pınar Mengüç for accepting to be a member of my defence committee.

I would like to thank the kids of İLKYAR. Seeing their enthusiasm towards education, science and arts made me believe once again that a bright future is in their hands. I am keeping my word to them and working hard to be a better academic one day. Finally, I would like to thank Prof. Hüseyin Vural for his impact on my intellectual development and teaching me that "our days are seeds in the hands of children." I have learned a lot from him.

Above all, I would like to thank my lovely wife, Ezgi Eriçok, for her tremendous patience on my constant nagging. She has been always helpful and supportive on my research. Thank you again for your encouragement when I needed it most. Thank you for being my best friend. I owe you a lot.

ABSTRACT

CHARACTERIZATION OF NANOPARTICLE AGGREGATES USING INVERSE FORMULATION AND DISCRETE-DIPOLE APPROXIMATION

Characterization of nanostructures using numerical light scattering experiments without using polarization information and a priori particle size or number measurements is investigated. Optimization and statistical methods are considered. The study focuses on particle clusters in the form of carbon nanoparticle aggregates generated with Filippov's particle-cluster algorithm. Mutually well separated nanoparticle aggregates with same size are assumed. The scattering behavior is calculated by discrete dipole approximation. A database is developed and used for the solution of the direct problem. First, the inverse problem is formulated as a least squares minimization. Use of Tabu Search along with gradient based Levenberg-Marquardt algorithm is investigated as problem topology is prone to multiple extrema. Then, the same problem is treated statistically and classical Bayesian inference methods and Approximate Bayesian Computation (ABC) methods are considered for the solution of the problem. Analytical likelihood function is obtained by additive noise assumption in classical Bayesian inference. On the other hand, four *likelihood-free* methods based on ABC that requires only simulation of the model without the need of evaluating a likelihood are considered. In particular, Rejection, Markov Chain Monte Carlo, Population Monte Carlo and Adaptive Population Monte Carlo are compared in terms of accuracy. All methods are able to predict the particle size and number for monodisperse aggregates with effective radius larger than 20 nm using a UV light source at a wavelength of 266 nm. Characterization of soot aggregates is performed with less than 2 nm deviation in nanoparticle radius and 3-4 deviation in number of nanoparticles forming the monodisperse cases. Promising results are also obtained for the characterization of polydisperse case.

ÖZET

TERS FORMULASYON VE AYRIK-DİPOL YAKLAŞIMI KULLANILARAK NANOPARÇACIK KÜMELERİNİN KARAKTERİZASYONU

Bu çalışmada nanoyapıların numerik ışık saçılım deneyleri ile karakterizasyonu çalışılmıştır. Polarizasyon bilgisi ya da önceden yapılmış çap ve boyut ölçümleri gerekmemektedir. Ele alınan problemin çözümünde eniyileme ve istatistiksel yöntemler kullanışmıştır. Bu çalışmanın odak noktası Filippov parçacık-küme algoritması ile oluşturulan karbon nanoparçacık kümeleridir.Bu kümelerin birbirlerinden yeterince uzakta oldukları ve aynı parçacık sayısına sahip oldukları varsayılmıştır. Nanoyapıların saçılım davranışları ayrık dipol yaklaşımı ile hesaplanmıştır. Ayrıca bir veritabanı oluşturularak sorunun çözümünde kullanılmıştır. İlk olarak, soru en küçük kareler eniyilemesi yöntemiyle kurgulanmıştır. Tabu Search ve Levenberg-Marquardt algoritmaları kullanılmıştır. Daha sonra, aynı problem klasik Bayesci sonuç çıkarımı ve yaklaşık Bayesci hesaplamalar ile çözülmüştür. Klasik Bayesci yaklaşımda olabilirlik fonksiyonu analitik olarak varsayılmıştır. Yaklaşık Bayesci hesaplamalar için, Geri Çevirme, Markov Zinciri Monte Carlo, Popülasyon Monte Carlo ve Uyarlayıcı Popülasyon Monte Carlo algoritmaları kullanılmıştır. Bütün hesaplamalar 266 nm ışıkla yapıldı. Etkin yarıçapın 20 nm'den büyük olduğu durumlarda bütün yöntemlerin başarılı sonuç verdiği görüldü. Ayrıca, parçacık yarıçapında dağılım olmadığı durumlarda, kurum parçacık yarıçapı ve sayısı sırasıyla 2 nm'den az ve 3-4 parçacık hassasiyetiyle tahmin edildi. Son olarak, parçacık yarıcapında dağılım olduğu durumlarda da umut verici sonuçlar elde edildi.

TABLE OF CONTENTS

LIST OF FIGURES

LIST OF TABLES

LIST OF SYMBOLS

$\mathbf{B}$	Reference point
$\mathbf{C}$	Center of the growing cluster
D_f	Fractal dimension
E	Random variable for error
$\mathbf{E}$	Measurement error
$\mathbf{E}_i$	Incident electric field
$\mathbf{E}_s$	Scattered electric field
F	Objective function
h	Acceptance probability
$\mathbf{H}_i$	Incident magnetic field
$\mathbf{H}_s$	Scattered magnetic field
I	Total intensity
I_{max}	Maximum number of iterations
$\mathbf{J}$	Jacobian matrix
$\mathbf{k}$	Wave vector
k_f	Fractal prefactor
$\mathbf{K}$	Stoke's vector
l	Distance between two centers
$l_{promising}$	Size of promising list
l_{tabu}	Size of tabu list
m	Refractive index
$\mathbf{M}$	Center of a sphere
$\hat{\mathbf{n}}$	Unit normal vector
N	Total number of points that will be sampled
N_m	Number of polar angles
N_n	Number of neighbors
N_p	Number of particles forming the aggregate
$\bar{N_p}$	Normalized domain for number of nanoparticles

p_{acc}	Acceptance rate
$p_{acc_{min}}$	Minimum acceptance rate
P	Random variable for $\mathbf{P}$
$\mathbf{P}$	Parameters of interest
q	Transition kernel
Q	Difference between horizontally and vertically polarized intensities
$Q(\alpha)$	α-quantile of a set
r_{eff}	Effective radius
r_n	Radius of neighbors
r_p	Primary particle radius
$\bar{r_p}$	Normalized domain for primary particle radius
r_{ps}	Radius of promising region
r_t	Radius of tabu region
R_g	Radius of gyration
s	A point in normalized parameter domain
S	Random variable for S_{ij}
S_j	Amplitude scattering matrix
S_{ij}	Mueller matrix
$\mathbf{S_{11}}^*$	Synthetic measurement
$\mathbf{S_{11}}(\mathbf{P})$	Scattering behavior of the aggregate defined by $\mathbf{P}$
t	Time
T	Number of iterations
U	Difference between $+45°$ and $-45°$ polarized intensities
V	Difference between the right-handed and left-handed circularly polarized intensities
$\mathbf{x}$	Coordinate of a point in space
α	Fraction of sampled points that will be stored
γ	Overlap condition
$\mathbf{\Gamma}$	Position of $\mathbf{M}$ relative to $\mathbf{C}$
ϵ	Tolerence

θ	Polar angle
λ	Wavelength
μ	Damping parameter
π_{pr}	Prior probability density
π_{post}	Posterior probability density
σ_r	Standard deviation in primary particle radii
Σ	Covariance matrix
ϕ	Azimuthal angle
$\mathbf{\Omega}$	Diagonal matrix of $\left(\mathbf{J}^k\right)$

LIST OF ACRONYMS/ABBREVIATIONS

GDI	Gasoline Direct Injection
NEDC	New European Driving Cycle
WLTC	Worldwide harmonized Light duty Test Cycle
TEM	Transmission electron microscopy
SEM	Scanning electron microscopy
AFM	Atomic force microscopy
TR-LII	Time-resolved laser-induced-incandescence
RDG	Rayleigh-Debye-Gans
RDG-FA	RDG for fractal aggregates
DDA	Discrete dipole approximation
DDSCAT	Discrete dipole scattering
ADDA	Amsterdam DDA
OpenDDA	OpenMP based DDA
DDA-SI-v	Discrete diple approximation with surface interactions vectorized version
WALS	Wide angle light scattering
MAP	Maximum a posteriori
ABC	Approximate Bayesian Computation
LM	Levenberg-Marquardt
TS	Tabu search
CTS	Continuous tabu search
ECTS	Enhanced continuous tabu search
DP	Direct problem
DB	Database
MCMC	Markov Chain Monte Carlo
PMC	Population Monte Carlo
APMC	Adaptive Population Monte Carlo

1. INTRODUCTION

Recent developments on the synthesis of nanoparticles have brought new opportunities to build new nanostructures, which have unique physical properties. These nanostructures are encountered in many diverse areas including biotechnology [1], medicine [2], combustion diagnostic systems [3–5]. In almost every case, characterization of these nanostructures is a very important task since the parameters such as size, shape and configuration have a great impact on the resulting physical properties or investigated physical phenomena. Black *et al.* [6] investigated the effects of ^{198}Au nanoparticle shape on their bio-distribution, tumor uptake and intratumoral distribution. They considered four different shapes (nanospheres, nanodisks, nanorods and cubic nanocages) with similar sizes and observed that the nanospheres exhibit the best blood circulation and tumor uptake. However, the nanorods and nanocages reached the core of the tumor better than nanospheres and nanodisks. The processes yielding these structures can be better understood through characterization of these shapes and optimization. Liati *et al.* [7] made a detailed analysis and characterization of soot particles emitted by a typical direct injection gasoline engine (GDI) vehicle during New European Driving Cycle (NEDC) and Worldwide harmonized Light duty Test Cycle (WLTC) at various temperature conditions and found that primary soot particles have diameter between 4-55 nm.

Synthesizing nanostructures with unique optical and physical properties necessitates new and improved characterization tools as manufacturing unique structures with desired properties is only possible through using proper characterization. There are different techniques for characterization of the size, shape and configuration of the nanostructures. Although the direct methods relying on microscopy such as transmission electron microscopy (TEM), scanning electron microscopy (SEM) and atomic force microscopy (AFM) are capable of producing high quality images [8], and are considered as the most reliable means of characterization, they usually are not suitable for in-line monitoring and they may damage the structure [9]. Time-resolved laser-induced-incandescence (TR-LII) is another method to characterize the size dis-

tribution of nanoparticles [10]. While it is possible to apply this method for in-situ characterization unlike electron microscopy, it is limited only to absorbing nanoparticles and although it is a promising technique there is need for further research to understand some challenging aspects such as the effect of particle composition on LII signals, effect of inhomogeneous particles, or important parameters such as accommodation coefficients related to nano-scale conduction models used for LII [11].

As an alternative, light scattering can be used for characterization of nanostructures. The challenge in light scattering techniques lies in the required rigorous analysis to model scattering of electromagnetic waves through nanostructures. Thus, relying on approximations is a frequently adopted approach. There are different methods to predict scattering behavior of aggregates in the literature. Rayleigh-Debye-Gans (RDG) approximation [12] and RDG for fractal aggregates (RDG-FA) [13, 14], are often used when the scatterer is irregularly shaped and smaller than the wavelength. RDG-FA is valid if $|m-1| \ll 1$ and $k|m-1|d_p \ll 1$ where m, k and d_p are the refractive index, wavenumber and primary particle diameter of aggregate. These approximations are often used to estimate the optical properties of combustion generated particles as in [15, 16]. However, Klusek *et al.* [17] stated that soot aggregates can not be treated as Rayleigh scatterers and Köylü and Faeth [18] stated that RDG-FA theory can not be used for soot aggregates with large refractive index. Besides these, they neglect the multiple and self-induced scattering effects and the error in angular scattering properties such as S_{11} and S_{12} can be as high as 50% for large aggregates [19]. T-matrix method [20–22], on the other hand, is a fast and accurate method to model scattering of light by aggregates. Although there is no limitation on primary particle size, T-matrix method is limited to non-overlapping spheres. In reality, aggregates may overlap and overlapping has an impact on scattering properties [23].

Discrete dipole approximation (DDA) is another method that is often used in the literature. The origins of DDA is rooted back to works of DeVoe [24,25] where DDA was applied to calculate the optical properties of molecular aggregates without considering the retardation effects. Couple of years later, Purcell and Pennypacker [26] introduced DDA with retardation effects and used it to study interstellar dust grains. DDA is a

semi-analytical volume integral method that can handle the most complex geometries by representing them with a finite set of interacting dipoles. Through the interactions of these dipoles, DDA can easily calculate the optical behavior of any geometry with any morphology. A detailed theoretical information can be found in [27]. As a widely adopted method, there are several open source codes available such as DDSCAT [28], ADDA [29], OpenDDA [30], and DDA-SI-v [31]. Though it can handle very complex geometries accurately it is slow compared to approximate methods [32].

In some applications light scattering and LII methods are combined. Riemann *et al.* [33] used LII method to estimate the soot primary particle radius and used that information as an input to ELS method to characterize radius of gyration. Once the primary particle radius and the radius of gyration are obtained the number of nanoparticles in the aggregate can be found from the fractal equation provided that the fractal parameters are known. Then, these values are compared to the TEM measurements and they observed a good agreement on primary particle radius, whereas the values of the radius of gyration and the number of nanoparticles shifted towards larger values. In another study, Huber *et al.* [34] used Wide-Angle Light Scattering (WALS) and TR-LII methods to find the radius of gyration and primary particle size of the fractal aggregates, respectively. RDG-FA theory is also used in more recent studies. For example, Liu *et al.* [35] used RDG-FA and generalized Mie-solution method to calculate the absorption and scattering properties of soot aggregates whereas Huber *et al.* [36] used WALS measurements and Bayesian inference to obtain credible intervals for size and morphology parameters of soot aggregates.

The Mueller matrix determined from the solution of the Maxwell's equations represents the exact scattering behavior of a scatterer by describing the relation between the incident light and scattered light. The matrix itself is a characteristic of a scatterer and a function of the scattering angle and the wavelength of the incident light. Therefore, if the Mueller matrix of a scatterer is known, a rigorous analysis considering its elements can be used for particle characterization via an inverse technique. Mengüç and Manickavasagam [37] reported that Mueller matrix elements with polarization information such as S_{12} and S_{34} can be used to estimate the number of nanoparticles in

the aggregate, N_p, and the primary particle radius, r_p . They outlined a procedure for determining the number of nanoparticles in the aggregate, provided that the primary particle radius is known via an ex-situ measurement such as via SEM. Charnigo *et al.* [38] used the normalized versions of S_{11}, S_{12}, S_{33} and S_{34} and their derivatives up to 5th degree to estimate the agglomeration level. They evaluated the performance of all the elements and their derivatives and found that relying on S_{33} yields the highest among them. In an another study, Charnigo *et al.* [39] used normalized versions of S_{12} and S_{33} and their derivatives to estimate the average nanoparticle diameter. They found that the nanoparticle diameter can be estimated within a 2 nm error if S_{33} is used.

The characterization of nanoparticle aggregates can be considered as a statistical problem as well. Statistical inversion based on Bayesian inference is a probabilistic approach, which is capable of predicting the probability distribution of the unknown parameters based on measurements. The basic idea of the Bayesian inference relies on updating the information about the unknown parameters based on the observations. Once the final probability distribution of the unknown parameters is obtained, credible intervals with a desired confidence level can be constructed.

Bayesian inference approach is relatively new for nanoparticle characterization. Burr *et al.* [40] used Bayesian inference to recover soot aggregate size distribution from multiangle elastic light scattering data using maximum a posteriori (MAP) inference. Sipkens *et al.* [41] used TR-LII method to characterize gas-borne silicon nanoparticles and analyzed their measurements with the Bayesian approach to find the most probable nanoparticle size distribution parameters. Otero *et al.* [42] studied the potentials of parametric and non-parametric Bayesian schemes on the inverse problems of light scattering. In another study, Clementi *et al.* [43] used Bayesian inversion method based on multidirectional dynamic light scattering measurements to estimate the particle size distribution of latexes. Charnigo *et al.* [44] used different elements of Mueller matrix and their derivatives to construct credible intervals for nanoparticle diameter and agglomeration level. They introduced both systematic and stochastic error in their analysis and utilized polarization information via normalized S_{11}, S_{12}, S_{33} and S_{34} for

different cases. In a more recent work, Hadwin *et al.* [45] used Bayesian inference to calculate the MAP and credible intervals of soot volume fraction and peak temperature for different likelihoods and priors densities whereas Huber *et al.* [36] used Bayesian inference to estimate the size and morphology parameters of soot-laden aerosols. Ericok and Erturk [46] used Bayesian inference for characterization of the radius and number of nanoparticles of the soot aggregates with different credible interval levels.

Computing the likelihood function is vital for Bayesian inference. However, it is not always available in a closed analytical form or feasible to compute due to complex physical models that require too many parameters. In general, there are three ways to overcome this problem: (1) Nonparametric estimation of the likelihood. In this method, one can run M auxiliary experiments based on the parameters that affect the outcome. The auxiliary experiments must be run at discrete points for a single parameter and intermediate points can be interpolated. However, if the number of parameters are not small this method suffers from what is known as "curse of dimensionality". (2) Parametric estimation of likelihood. One can assume an analytical form, e.g. Gaussian or Poisson distributions, for likelihood. Although this method is very practical it may misrepresent the physical reality. (3) Parametric estimation after dimension reduction. This method does not use whole outcome of the system but its sufficient statistics. If there exist a sufficient statistics such as mean, standard deviation etc. that represents the outcome well one may reduce the number of unknowns and use parametric estimation on the reduced unknowns. More information can be found in [44].

One alternative way to cope with this problem is not using likelihood altogether. If likelihood is not available or can not be obtained by the methods described above Bayesian inference is performed via what is known as Approximate Bayesian Computation (ABC) techniques. ABC consists of methods that do not require the calculation of the likelihood function to obtain the posterior distribution. The idea is to sample points from the posterior distribution directly if there exists a model that relates the parameters of interest to observable quantities. While ABC methods are widely used in different fields such as genetics [47], epidemiology [48], cosmology [49] and signal detection theory [50] etc., they have not been used for solution of inverse radiative

transfer and optical characterization problems.

In radiative transfer and optical characterization, Bayesian inference methods are generally performed by assuming an analytical form to the likelihood function as in [40–46]. However, most of the problems considered are complex, where the physical behavior of the system can not be represented by an analytical expression necessitating the use of numerical modeling. For the analysis of such problems using ABC methods is a more reasonable approach. In this study, some of the ABC methods will be introduced for the first time to our best knowledge and applied rigorously for characterization of nanoparticle aggregates to demonstrate the strengths and limitations of the proposed methods.

The current state of the art allows light scattering methods to be used in characterization with polarization information and a priori ex-situ or in-situ measurement via SEM or LII. This thesis aims to extend the current state of the art by investigating the feasibility of simultaneous estimation of the number of particles and the primary radius, N_p and r_p, of a soot aggregate without using any polarization information or relying on a priori measurement. Suspended soot aggregates are considered as an example and numerical experiments are used in this study.

In this thesis, characterization of nanoparticle aggregates via different optimization techniques and statistical approaches is investigated. Each of these methods are explained and tested in great details and the results are presented in corresponding chapters. In Chapter 2, the electromagnetic theory of optical scattering is reviewed briefly. After that, representation of nanoparticle aggregates are explained in Chapter 3. In Chapter 4, the problem definition and some useful concepts are introduced. Characterization of nanoparticle aggregates with optimization methods and statistical approaches are explained in Chapters 5 and 6, respectively.

2. ELECTROMAGNETIC THEORY OF OPTICAL SCATTERING

Light is an electromagnetic wave that can interact with matter. This interaction may occur with different physical events such as absorption or scattering. When the matter is illuminated by light electrons and protons of the matter are excited and set into oscillatory motion. Because of the accelerated electric charges some amount of electromagnetic energy is released in every direction. This event is known as scattering. Moreover, some amount of the incoming electromagnetic energy may be transformed into thermal energy by a process known as absorption. In this chapter, the physical foundations and the mathematical formulations of the scattering event will be introduced.

2.1. General Formulation

In this section, the mathematical formulation of the scattering event will be gradually developed by considering an arbitrary object with known shape, size and optical properties illuminated by arbitrarily polarized monochromatic wave. If the electric and magnetic fields are determined for all points within the object and the surrounding medium the solution of the scattering event is obtained.

Figure 2.1 shows the scattering event caused by an arbitrary object. The incident and scattered electromagnetic fields are denoted by subscripts i and s, respectively. Moreover, the fields inside and outside of the object are denoted by subscripts 1 and 2. The field outside the object is comprised of the incident and scattered fields, and can therefore be written as the sum of these fields.

$$\mathbf{E}_2 = \mathbf{E}_i + \mathbf{E}_s \tag{2.1a}$$

$$\mathbf{H}_2 = \mathbf{H}_i + \mathbf{H}_s \tag{2.1b}$$

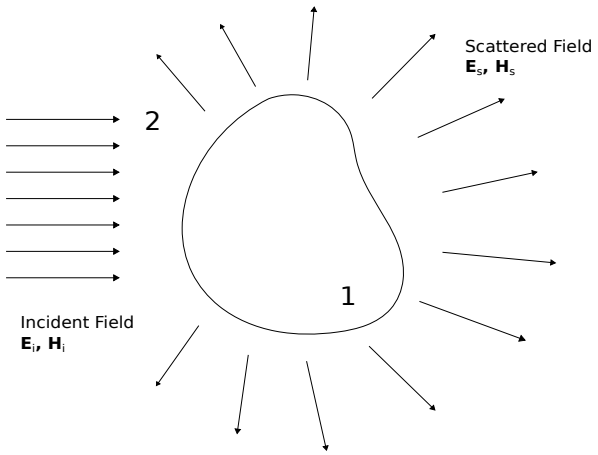

Figure 2.1. Schematic of the scattered ($\mathbf{E}_s$, $\mathbf{H}_s$) and internal ($\mathbf{E}_1$, $\mathbf{H}_1$) electromagnetic field caused by the incident electromagnetic field ($\mathbf{E}_i$, $\mathbf{H}_i$) upon an object with arbitrary shape.

Incident electromagnetic fields in Equation 2.1 are considered as plane harmonic waves with,

$$\mathbf{E}_i = \mathbf{E}_0 \, e^{i(\mathbf{k}\cdot\mathbf{x} - wt)} \tag{2.2a}$$

$$\mathbf{H}_i = \mathbf{H}_0 \, e^{i(\mathbf{k}\cdot\mathbf{x} - wt)} \tag{2.2b}$$

where $\mathbf{k}$ and $\mathbf{x}$ represent the wave vector and a coordinate of a point in space, respectively.

The scattering event is governed by the Maxwell's equations,

$$\nabla \cdot \mathbf{E} = 0 \tag{2.3a}$$

$$\nabla \cdot \mathbf{H} = 0 \tag{2.3b}$$

$$\nabla \times \mathbf{E} = i\omega\mu\mathbf{H} \tag{2.3c}$$

$$\nabla \times \mathbf{H} = -i\omega\epsilon\mathbf{E} \tag{2.3d}$$

where ϵ and μ are electric permittivity and permeability, respectively. Note that these properties are continuous functions. However, there may have a sudden change in these

functions at the boundary of the object due to the differences in optical properties of object and the surrounding medium. Therefore, the following boundary conditions are imposed:

$$[\mathbf{E}_2(\mathbf{x}) - \mathbf{E}_1(\mathbf{x})] \times \hat{\mathbf{n}} = 0 \tag{2.4a}$$

$$[\mathbf{H}_2(\mathbf{x}) - \mathbf{H}_1(\mathbf{x})] \times \hat{\mathbf{n}} = 0 \tag{2.4b}$$

where $\hat{\mathbf{n}}$ is the unit normal vector pointing outwards of the surface of the object. If the fields given in Equation 2.2 satisfy the Maxwell's equations given in Equation 2.3 with appropriate boundary conditions the scattered electromagnetic fields can be determined for all points inside and outside of the object. The boundary conditions given in Equation 2.4 guarantee that the tangential components of the electric and magnetic fields across the boundary are continuous.

2.2. The Amplitude Scattering Matrix

Figure 2.2 shows an arbitrarily shaped particle illuminated by an electromagnetic wave. The object is located at the origin of a Cartesian coordinate frame whose unit vectors are denoted as $\hat{\mathbf{e}}_x$, $\hat{\mathbf{e}}_y$ and $\hat{\mathbf{e}}_z$. The *forward direction* is defined as the direction of propagation of the incident wave, represented by z-axis in our case. The direction of the scattered wave is shown with unit vector $\hat{\mathbf{e}}_r$. The combination of the forward and scattered directions defines the scattering plane shown as grids in Figure 2.2.

Using Equation 2.2, the incident wave becomes

$$\mathbf{E}_i = \left(E_{0\parallel}\hat{\mathbf{e}}_{\parallel i} + E_{0\perp}\hat{\mathbf{e}}_{\perp i}\right)\exp^{i(kz-\omega t)} = E_{\parallel i}\hat{\mathbf{e}}_{\parallel i} + E_{\perp i}\hat{\mathbf{e}}_{\perp i} \tag{2.5}$$

where $E_\parallel$ and $E_\perp$ are the parallel and perpendicular components of the electric field, respectively. k in Equation 2.5 is the wavenumber with $k = 2\pi m/\lambda$ where m and λ are the refractive index and wavelength of the incident wave in vacuum, respectively.

The scattered field in the far-field region ($kr \gg 1$) can be approximated as transverse ($\hat{\mathbf{e}}_\mathbf{r} \cdot \mathbf{E}_s = 0$), and is shown to have asymptotic form [51]

$$\mathbf{E}_s \approx \frac{\exp^{ikr}}{-ikr}\mathbf{A} \tag{2.6}$$

with $\hat{\mathbf{e}}_\mathbf{r} \cdot \mathbf{A} = 0$. This feature allows us to write scattered field as

$$\mathbf{E}_s = E_{\parallel s}\hat{\mathbf{e}}_{\parallel s} + E_{\perp s}\hat{\mathbf{e}}_{\perp s} \tag{2.7}$$

Considering all, the scattered electric field is related to incident electric field by a 2×2 matrix [52]

$$\begin{pmatrix} E_{\parallel s} \\ E_{\perp s} \end{pmatrix} = \frac{e^{ik(r-z)}}{-ikr} \begin{pmatrix} S_2 & S_3 \\ S_4 & S_1 \end{pmatrix} \begin{pmatrix} E_{\parallel i} \\ E_{\perp i} \end{pmatrix} \tag{2.8}$$

The matrix formed by the elements S_j ($j = 1, 2, 3, 4$) is known as the *amplitude scattering matrix*. The elements S_j are functions of the scattering angle, θ, and azimuthal angle, ϕ.

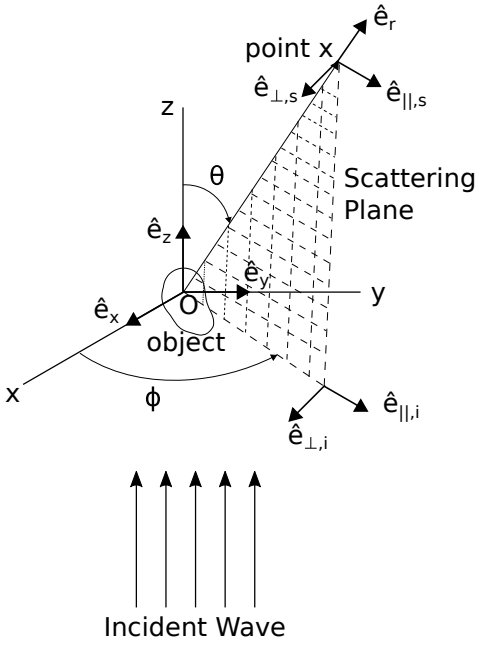

Figure 2.2. Schematic of the scattering plane.

2.3. Mueller Matrix

While performing experiments measuring $E_{\parallel}$ and $E_{\perp}$ is harder than measuring the time averaged value of the amplitude square. Therefore, scattering event is usually formulated with easily measurable quantities such as intensity, rather than amplitudes of electric fields. Stokes showed that 4 elements are enough to fully describe the intensity and polarization state of an electromagnetic wave.

$$\mathbf{K} = \begin{pmatrix} I & Q & U & V \end{pmatrix}^T \tag{2.9}$$

The Stokes vector, $\mathbf{K}$, in Equation 2.9 contains information of the total intensity, I, difference between horizontally and vertically polarized intensities, Q, difference between $+45^\circ$ and -45° polarized intensities, U, and the difference between the right-handed and left-handed circularly polarized intensities, V with $I^2 = Q^2 + U^2 + V^2$ [52]. The scattered stokes vector are related to the amplitude of the electric field by,

$$I_s = \langle E_{\parallel s} E^*_{\parallel s} + E_{\perp s} E^*_{\perp s} \rangle \tag{2.10a}$$

$$Q_s = \langle E_{\parallel s} E^*_{\parallel s} - E_{\perp s} E^*_{\perp s} \rangle \tag{2.10b}$$

$$U_s = \langle E_{\parallel s} E^*_{\perp s} + E_{\perp s} E^*_{\parallel s} \rangle \tag{2.10c}$$

$$V_s = i\langle E_{\parallel s} E^*_{\perp s} - E_{\perp s} E^*_{\parallel s} \rangle \tag{2.10d}$$

With Stokes vector, the incident and scattered intensities can be related to each other by [52],

$$\begin{pmatrix} I_s \\ Q_s \\ U_s \\ V_s \end{pmatrix} = \frac{1}{k^2 r^2} \begin{pmatrix} S_{11} & S_{12} & S_{13} & S_{14} \\ S_{21} & S_{22} & S_{23} & S_{24} \\ S_{31} & S_{32} & S_{33} & S_{34} \\ S_{41} & S_{42} & S_{43} & S_{44} \end{pmatrix} \begin{pmatrix} I_i \\ Q_i \\ U_i \\ V_i \end{pmatrix} \tag{2.11}$$

where the 4×4 matrix relating the incident and scattered Stokes vectors is known as the *scattering* or *Mueller matrix*. All the elements of the Mueller matrix are functions

of the scattering angle, θ, and the wavelength of the incident light, λ.

Finally, the relation between the Mueller matrix and and the amplitude scattering matrix is given by,

$$
\begin{aligned}
S_{11} &= \frac{1}{2}\left(|S_1|^2 + |S_2|^2 + |S_3|^2 + |S_4|^2\right) \\
S_{12} &= \frac{1}{2}\left(|S_2|^2 - |S_1|^2 + |S_4|^2 - |S_3|^2\right) \\
S_{13} &= Re\{S_2 S_3^* + S_1 S_4^*\} \\
S_{14} &= Im\{S_2 S_3^* - S_1 S_4^*\} \\
S_{21} &= \frac{1}{2}\left(|S_2|^2 - |S_1|^2 - |S_4|^2 + |S_3|^2\right) \\
S_{22} &= \frac{1}{2}\left(|S_2|^2 + |S_1|^2 - |S_4|^2 - |S_3|^2\right) \\
S_{23} &= Re\{S_2 S_3^* - S_1 S_4^*\} \\
S_{24} &= Im\{S_2 S_3^* + S_1 S_4^*\} \\
S_{31} &= Re\{S_2 S_4^* + S_1 S_3^*\} \\
S_{32} &= Re\{S_2 S_4^* - S_1 S_3^*\} \\
S_{33} &= Re\{S_1 S_2^* + S_3 S_4^*\} \\
S_{34} &= Im\{S_2 S_1^* + S_4 S_3^*\} \\
S_{41} &= Im\{S_2^* S_4 + S_3^* S_1\} \\
S_{42} &= Im\{S_2^* S_4 - S_3^* S_1\} \\
S_{43} &= Im\{S_1 S_2^* - S_3 S_4^*\} \\
S_{44} &= Re\{S_1 S_2^* - S_3 S_4^*\}
\end{aligned}
$$

The definition of each individual element of Mueller matrix may help better understand the scattering event. S_{11} represents the differential scattering cross section. If an unpolarized light is incident upon the particle, $\mathbf{K}_i = \begin{bmatrix} 1 & 0 & 0 & 0 \end{bmatrix}$, then S_{11} relates the incident total intensity, I_i, to scattered total intensity, I_s by $S_{11} = I_s/I_i$ with $(kr)^{-2}$ omitted. An equivalent representation is the scattering phase function if it is normalized by the area under $S_{11} - \theta$ curve [52].

3. REPRESENTATION OF AGGREGATES

The characterization of nanoparticle aggregates based on their light scattering behavior via numerical experiments is studied in this work. In this chapter, the numerical aggregate generation procedure is explained.

3.1. Fractal-Like Aggregates

Aggregates can be mathematically represented using the fractal equation,

$$N_p = k_f(R_g/r_p)^{D_f} \tag{3.1}$$

where N_p is the number of particles in the aggregate, r_p is the primary particle radius, R_g is the radius of gyration, and D_f and k_f are the fractal dimension and fractal prefactor, respectively. At the limits, $D_f = 1$ represents the case where the particles are all perfectly aligned, whereas $D_f = 3$ represents the case that they form a perfect sphere.

Fractal-like aggregates can be generated by the Filippov's algorithm [53]. There are two main approaches regarding the simulation of the aggregate formation. The particle-cluster algorithm starts with two touching particles and adds one particle at a time to the cluster of nanoparticles. Whereas, in the cluster-cluster algorithm, there are small aggregates with more or less equal number of primary particles. At each step, these small clusters are connected to each other in a specific way to create one big aggregate. Although cluster-cluster method produces more realistic fractals it fails to create fractals with higher dimensions [54]. Therefore, the particle-cluster algorithm is used in this work.

3.2. Filippov's Particle-Cluster Algorithm

Filippov's particle cluster algorithm starts with two spheres in point contact. Although there are several ways to generate the coordinates of such spheres Marsaglia's approach [55] shown in Figure 3.1 is adopted here. Marsaglia's approach finds the coordinates of the second sphere while the first one is assumed to be located at the origin, $\mathbf{R_1} = 0\hat{\mathbf{i}} + 0\hat{\mathbf{j}} + 0\hat{\mathbf{k}}$. Here, r_1 and r_2 must be supplied as the radii of the each sphere and u and v are uniform random numbers sampled from the interval $[-1, 1]$. At the end, the coordinates of two spheres in point contact are obtained as $\mathbf{R_1}$ and $\mathbf{R_2}$. Suppose a fractal with $N_p = 100$ particles will be generated with Filippov's algorithm.

given r_1 and r_2
while $S \geq 1$ **do**
  generate random numbers u and v from $[-1, 1]$
  calculate $S = u^2 + v^2$
end while
calculate $\bar{\mathbf{R}}_\mathbf{2} = 2u(1-S)^{1/2}\hat{\mathbf{i}} + 2v(1-S)^{1/2}\hat{\mathbf{j}} + (1-2S)\hat{\mathbf{k}}$
calculate coordinate of the second sphere as $\mathbf{R_2} = (r_1 + r_2) \times \bar{\mathbf{R}}_\mathbf{2}$

Figure 3.1. Marsaglia's algorithm to choose a point from the surface of a sphere.

After the coordinates of initial two spheres are found the coordinates of the remaining particles need to be found while satisfying Equation 3.1. In order to find the exact coordinates, the distance between the center of each sphere, $\mathbf{M}$, and the geometrical center of cluster at the current step, $\mathbf{C}$, must be determined first with the Equation 3.2 shown below.

$$|\mathbf{\Gamma}|^2 = \frac{n^2 r_p^2}{n-1}\left(\frac{n}{k_f}\right)^{\frac{2}{D_f}} - \frac{n r_p^2}{n-1} - n r_p^2 \left(\frac{n-1}{k_f}\right)^{\frac{2}{D_f}} \tag{3.2}$$

where $\mathbf{\Gamma}$ is the position of $\mathbf{M}$ relative to $\mathbf{C}$ whereas n in Equation 3.2 represents the current step where $n = 3...N_p$.

The distance $|\mathbf{\Gamma}|$ represents a spherical surface (shown in thick line in Figure 3.2) that may intersect more than one particle of the growing cluster. The possible

particles that the new particle may interact are shown as dark gray spheres in Figure 3.2 and the new particle can be attached to the surface of any of them without violating Equation 3.1. Therefore, a list of these dark gray particles must be kept at each step and the particle that the new one will interact must be selected randomly. The list, *ListPossible*, contains of particles located at least $|\mathbf{\Gamma}| - 2r_p$ away from the center of the cluster.

Once the *ListPossible* is obtained one particle must be selected randomly from the list as a reference point. This reference point, **B**, will be used to define angles α and β shown in Figure 3.2. α represents the angle $\angle ACB$ of the ACB triangle and can be calculated using Cosine theorem with lengths $|CA| = |\mathbf{\Gamma}|$, $|AB| = 2r_p$ and $|CB|$. On the other hand, β defines the rotation of $\mathbf{\Gamma}$ around axis **CB** and must be determined randomly.

After all the necessary lengths and angles are determined the overlap condition which ensures that the new particle does not intersect with the rest of the cluster must be checked. The overlap condition, γ, defined in Equation 3.3 is suggested to be less than 10^{-8} in [54]. If the overlap condition is not met for a randomly selected β a new β should be selected randomly. However, if the overlap condition is not met for a predetermined number of β trials (for example, 25) a new reference point should be selected from the *ListPossible* and all the calculations should be repeated. It should be noted that all the rotations mentioned here can be performed easily with the quaternion rotations, that will be explained briefly in the upcoming sections.

$$\gamma = 1 - \frac{l}{2r_p} \tag{3.3}$$

where l is the distance between the two centers. Noteice that this condition must be checked not only for reference point, but also for the points in the *ListPossible*.

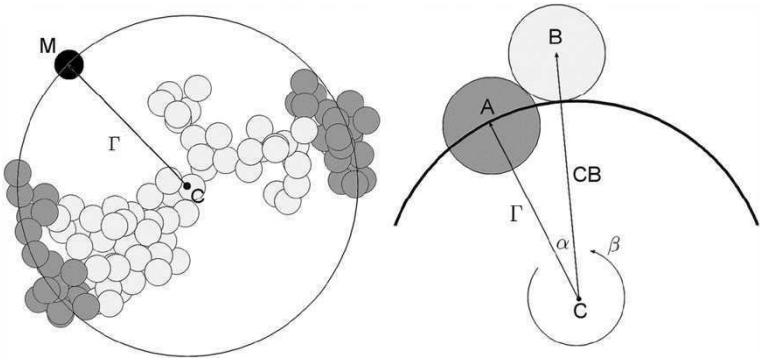

Figure 3.2. Schematic of the aggregation process. **C** and **M** are the center of the cluster and the current sphere, respectively. **Γ** is the distance between **C** and **M**. A and B show the current and reference point, respectively. Image is taken from (Skorupski *et al.*, 2014).

given $\mathbf{R_1}$, $\mathbf{R_2}$, N_p, D_f and k_f
for $n > 2$ **do**
  calculate $|\mathbf{\Gamma}|$ using Equation 3.2
  determine *ListPossible*
  while $\gamma > 10^{-8}$ **do**
    select a reference point from *ListPossible* randomly
    calculate α
    for $trials = 1$ to $MaxTrials = 25$ **do**
      select β randomly from uniform $[0, 1]$
      perform quaternion rotation
      calculate γ for every point in *ListPossible* with Equation 3.3
      if $\gamma < 10^{-8} \,|\, \forall\gamma$ **then**
        break
      end if
    end for
  end while
end for

Figure 3.3. Filippov's particle-cluster algorithm described briefly.

The Filippov's particle-cluster algorithm described in Figure 3.3 possess randomness that manifests itself in the aggregates generated. Two different aggregates generated with Filippov's particle-cluster algorithm are presented in Figure 3.4. Both aggregates contain 100 particles with morphology parameters $D_f = 1.81$ and $k_f = 1.37$. Their shapes are different due to the randomness of Filippov's algorithm even though all the parameters defining the two aggregates are identical. This observation will be taken into account in calculations.

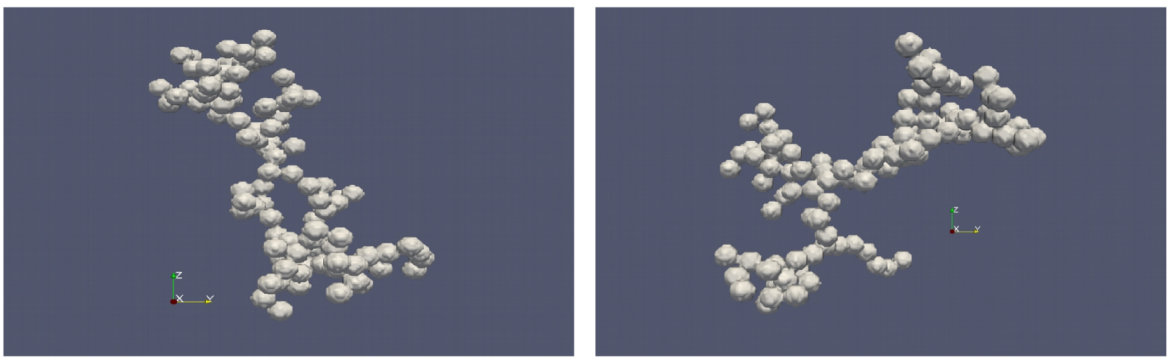

Figure 3.4. Two different sample aggregates of 100 particles with $D_f = 1.81$ and $k_f = 1.37$ from the same view angle.

4. PROBLEM STATEMENT

4.1. Description of Measurement Volume and Assumptions

Characterization of nanoparticle aggregates using elastic light scattering techniques is studied in this work. In particular, soot aggregates left from incomplete combustion are considered as an example because of the enormous knowledge available in the literature. Before going into details some important concepts will be introduced.

In a real time light scattering experiment, the measurement volume comprises of aggregates with different morphological and optical properties. These aggregates often contain different numbers of primary particles, and the radii of primary particles per aggregate are not constant. A light scattering experiment measures the scattering behavior of a this kind of ensemble and a researcher uses this experimental data to retrieve the desired properties or parameters.

The characterization of soot aggregates using numerical light scattering experiments is studied in this work as an example. Characterization of soot aggregates means retrieving all the necessary information about the aggregates present at the measurement volume using their scattering behaviour. The unknowns of this problem include refractive index of soot, distribution of radius and size of the primary particles, fractal parameters etc. However, the inverse light scattering problem of this kind is almost impossible to solve and people often simplify the problem by assumptions. In the characterization of light scattering literature, the numerical studies generally ignore the diversity in refractive index of soot and assume it constant [56, 57] although Bond and Bergstorm showed that there is a huge uncertainty in the refractive index of soot [58]. In this study, the refractive index of soot is adopted from [59].

The fractal parameters, D_f and k_f, which are used to define a fractal mathematically, substantially affect the absorption and scattering behavior of soot aggregates [17, 22, 60]. The values of these parameters are also assumed known and constant

in some studies. Different authors suggest different values for D_f and k_f for soot aggregates. The typical value of D_f is around 1.7-1.8 [61, 62]. However, there is no general consensus about the value of k_f. Yon *et al.* [59] calculated these values from the results of two independent experiments and they reported that $D_f = 1.81$ and $k_f = 1.37$. Therefore, these values are considered as input to the aggregate generation algorithms.

Finally, if the refractive index and the fractal parameters are considered as known the only unknowns are primary particle radii and the aggregate size. A typical value for the radius of a primary particle constituting the soot aggregate is considered to be less than 25 nm [60]. However, a range of 5 nm to 50 nm is also suggested [17]. On the other hand, the range of total number of particles forming the aggregate is quite large, and being less than 1000 particles [56]. However, relatively small number of particles are used in the literature, for examples Wu *et al.* [63] used soot aggregates with 100 particles in their simulations. Moreover, Tian *et al.* [64] presented a probability distribution for number of nanoparticles per aggregate based on an experimental study and showed that the probability of aggregates having $N_p < 30$ is higher than others.

The effective radii of the aggregates are calculated based on Equation 4.1. It is simplified to $r_{eff} = r_p N_p^{1/3}$ for aggregates with constant radii.

$$r_{eff} = \left(\sum_{i=1}^{N_p} r_i^3 \right)^{1/3} \tag{4.1}$$

In this work, measurement volumes containing aggregates with monodisperse and polydisperse radii distribution of non-overlapping spheres are considered. If these aggregates are similar to each other and they form a dilute suspension the scattering behavior of the the ensemble can be simulated with the scattering behavior of a single aggregate averaged over multiple orientations as considered in [32, 65–68]. Orientation averaging compensates for the effects of random orientations of many aggregates as well as the movement of these aggregates during the measurement time.

4.2. Simulation of Scattering Behavior of Aggregates

Obtaining the scattering behavior of a given aggregate with known geometry and morphology requires the solution of the direct problem by solving the Maxwell's equations. Since an analytical solution of the Maxwell's equation for a complex geometry such as an aggregate is not available, use of numerical methods are required. In this thesis, Fortran implementation of DDA, DDSCAT developed by Draine and Flatau [28], is used for the solution of the direct problem.

4.3. Synthetic Measurements

The objective of the current study is to examine the validity of the proposed methods via numerical experiments. Therefore, the actual experimental measurements are replaced with synthetic measurements that are obtained by adding random measurement error to the simulated scattering behavior of known ensemble of aggregates. Solution of the direct problem depends on the geometrical orientation of the aggregate with respect to the direction of incident radiation. Therefore, while producing the simulated measurements, the solution of the direct problem is averaged for 490 different orientations of the aggregate relative to the incident light as recommended in [37], in order to avoid such dependency.

For the monodisperse cases, it is well known that the scattering phase function (hence S_{11}) of the ensemble of randomly oriented soot aggregates can be approximated by the scattering behavior of a single aggregate averaged over adequate orientations [68]. Therefore, synthetic measurements can be created by the scattering behavior of a single aggregate averaged over multiple orientations.

The scattering behavior of the ensemble of polydisperse aggregates, on the other hand, can not be approximated by the scattering behavior of a single aggregate because of the large variations in primary particle radii among different aggregate realizations. This is especially true when the number of particles forming the aggregate is small. In these cases, scattering behavior of multiple aggregate realizations must be averaged

to represent the scattering behavior of the ensemble. Our preliminary analysis showed that taking an average over 40 realizations is sufficient to represent the scattering behavior of the ensemble.

Equation 4.2 below shows how syntehetic measurements are created.

$$\mathbf{S_{11}}^{*}_{i,j} = \mathbf{S_{11}}_{i}(N_p, r_p, \sigma_r) + \mathbf{E}_{i,j}(\mu = 0, \sigma = 10^{-4}) \tag{4.2}$$

where i and j are the indices of ensemble and error, respectively. The measurement error is assumed to have a normal distribution with a known standard deviation of $\sigma = 10^{-4}$, considering the uncertainty of a commercial device [69].

As mentioned in Chapter 3, every fractal geometry generated with exactly the same parameters will be different due to the randomness of the algorithm. Therefore, this effect should also be taken into account while constructing the synthetic measurements. 10 and 100 aggregate realizations are created for a given monodisperse and polydisperse cases, respectively.

Moreover, the measurement error may also have some impact on the final results. Therefore, 10 different random error vectors are introduced to the scattering profile of each ensemble created for each monodisperse case. As a result, 100 different synthetic measurements (10 different measurement error to each of 10 ensembles) are obtained with Equation 4.2 for each monodisperse case whereas a single synthetic measurement is obtained for each polydisperse case by averaging the simulated measurements obtained by adding random measurement to the scattering behavior of each 100 aggregate realizations.

The physical limitations of the actual experimental setup must be taken into account. The measurements at $\theta = 0^\circ$ and $\theta = 180^\circ$ are not possible in the same plane. Moreover, measurements near these angles are highly disturbed by the incident light. Considering these limitations, the initial and and final polar angles are taken as $\theta_i = 5^\circ$ and $\theta_f = 165^\circ$, respectively. In our study [70], we have shown that the increment

between these angles may not affect much the results of characterization if $\Delta\theta < 16°$. Therefore, the scattering profiles of every parameters set contain measurements between $\theta_i = 5°$ and $\theta_f = 165°$ with $\Delta\theta = 8°$.

At the end, the proposed method relies on measurements of $\mathbf{S_{11}}^*$ for a given aggregate at N_m polar angles; $\theta_i, i = 1..N_m$. The inverse problem can then be defined as predicting the aggregate that would yield these measurements, $\mathbf{S_{11}}^* = [S_{11}^*(\theta_1) \dots S_{11}^*(\theta_m)]^T$ where N_m is the number of polar angles.

4.4. Database

The computational time required for a direct solution using DDSCAT for a single set of N_p and r_p, averaging 490 orientations is computationally demanding. Solution of such a problem for an aggregate of 15 nanoparticles with a radius of 8 nm, using a total of 4734 dipoles requires 787 seconds in an 8 core system with 2.50 GHz frequency, using a parallel implementation of DDSCAT. The required computation time increases as the number and size of particles in the aggregate increase due to increasing number of dipoles simulated. Moreover, it is well known that stochastic methods usually necessitate high number of iterations, whereas the gradient based methods require the estimation of Jacobian that might also be computationally demanding. Therefore, solution of an inverse problem necessitating high number of iterations might not be computationally feasible due to significant computation time required for every iteration.

A common practice for solution of similar problems is to establish a database for different configurations and using the information available in the database for optimization [37, 71]. Therefore, a database was created considering fifteen different numbers of particles ranging from 3 to 45 with an increment of 3. Similarly, fifteen different particle radii ranging from 3 nm to 45 nm with an increment of 3 nm were considered, assuming that every nanoparticle in the aggregate has the same radii. For each particle size and number combination, twelve different fractal-like nanoparticle aggregates were generated using the particle-cluster algorithm. The resulting geome-

tries are slightly different from each other due to the randomness of the algorithm. For a given N_p and r_p combination, orientation averaged S_{11} are estimated by DDSCAT considering 490 orientations as explained earlier, for all twelve geometries. Therefore, every S_{11} value for a particular scattering angle in the database is the average of 5880 simulations (490 orientations each for 12 different fractal geometries). Moreover, the scattering angles considered while constructing the database range from 0° to 180° with 1° increment, allowing us to use any subinterval with any increment. The database developed for this study is comprised of a total of 225 (15 different numbers of particles and 15 different particle sizes) set of parameters, and cubic splines were used for prediction of intermediate variables. It should be noted that the database can be extended easily for developing a tool capable of providing a solution in a larger domain.

5. CHARACTERIZATION OF NANOPARTICLE AGGREGATES WITH OPTIMIZATION METHODS

In this chapter, characterization of nanoparticle aggregates with optimization methods is studied. The inverse problem considered is formulated as a non-linear least square minimization. Deterministic methods such as Levenberg-Marquardt and Conjugate Gradient Methods use the gradient information and usually converge relatively faster. However, the problem considered may contain multiple local minima, and predicting the global minimum is not guaranteed by using these methods relying on gradient information. Although stochastic methods or meta-heuristics are usually computationally expensive, they have superior performance in locating a global minimum. Simulated Annealing, Genetic and Tabu Search algorithms are widely used stochastic methods in the literature. This study considers using Levenberg-Marquardt and Tabu Search for the solution of the inverse problem.

5.1. Test Cases

The cases considered in this chapter are selected to identify the strengths and the limitations of the method considering the physical limitations explained in Section 4.1, and they are presented in Table 5.1.

The cases considered have effective radius ranging between 15.8 nm to 121.5 nm. Cases with smaller particle size and number are considered to test the lower limit of characterization since the values of S_{11} tend to approach the measurement uncertainty as size of the aggregates get smaller. While Cases 1-7 consider monodisperse aggregates comprised of uniform sized particles, the last case, Case 8, considers a polydisperse aggregate comprised of particles having a log-normal size distribution. Therefore, the solution for this case necessitates the prediction of standard deviation along with mean particle size and particle number. The number of particles, mean particle size, and the standard deviation for this case is selected based on data presented [10].

Table 5.1. The cases to test the validity of the proposed inverse method.

Cases	**Mean particle radius** r_p [nm]	**Number of particles** N_p	**Deviation** σ_r	**Effective radius** r_{eff} [nm]
Case 1	33.5	17	0	86.1
Case 2	12.0	8	0	24.0
Case 3	19.0	12	0	43.5
Case 4	26.0	22	0	72.8
Case 5	40.0	28	0	121.5
Case 6	10.0	4	0	15.8
Case 7	10.0	7	0	19.1
Case 8	15.0	30	1.25	50.3

5.2. Optimization Methods

The inverse problem is formulated as a non-linear least squares minimization problem and its solution requires using optimization methods. In this work, Levenberg-Marquardt and Tabu Search algorithms are used as examples of gradient-based and stochastic optimization methods, respectively.

5.2.1. Objective Function

As the fractal dimension and prefactor are approximately known for soot aggregates, the system can be defined in terms of parameters $\mathbf{P} = [N_p \; r_p \; \sigma_r]^T$. Then, the inverse problem can be defined as estimation of these parameters that minimizes the objective function,

$$F(\mathbf{P}) = |\mathbf{S_{11}}^* - \mathbf{S_{11}}(\mathbf{P})|^2 \tag{5.1}$$

where $\mathbf{S_{11}}^*$ and $\mathbf{S_{11}}(\mathbf{P})$ represent the synthetic measurement and the estimation of S_{11} for a given set of variables $\mathbf{P}$, respectively.

5.2.2. Levenberg-Marquardt (LM) Algorithm

LM algorithm is a widely used iterative method, which is capable of solving ill-conditioned nonlinear least squares problems of parameter estimation using gradient information. Theoretical information and some applications of the method can be found in [72, 73]. The objective function defined in Equation 5.1 can be rewritten as,

$$F(\mathbf{P}) = \left[\mathbf{S_{11}}^* - \mathbf{S_{11}}(\mathbf{P})\right]^T \left[\mathbf{S_{11}}^* - \mathbf{S_{11}}(\mathbf{P})\right] \tag{5.2}$$

where $\mathbf{P} = [N_p \ r_p \ \sigma_r]^T$ denotes the unknown vector. The objective of the LM algorithm is to minimize the Equation 5.2. Mathematically, the solution is located (if exists) at the minima of the objective function. Therefore, the derivatives of the objective function with respect to the unknown parameters must be zero.

$$\nabla F\left(\mathbf{P}\right) = 2\left[\frac{-\partial \mathbf{S_{11}}^{\mathbf{T}}(\mathbf{P})}{\partial \mathbf{P}}\right]\left[\mathbf{S_{11}}^* - \mathbf{S_{11}}(\mathbf{P})\right] = 0 \tag{5.3}$$

Then, the Jacobian matrix, $\mathbf{J}$, is defined as,

$$\mathbf{J}(\mathbf{P}) = \left[\frac{\partial \mathbf{S_{11}}^{\mathbf{T}}(\mathbf{P})}{\partial \mathbf{P}}\right] = \begin{pmatrix} \frac{\partial S_{11,1}}{\partial N_p} & \frac{\partial S_{11,1}}{\partial r_p} & \frac{\partial S_{11,1}}{\partial \sigma_r} \\ \frac{\partial S_{11,2}}{\partial N_p} & \frac{\partial S_{11,2}}{\partial r_p} & \frac{\partial S_{11,2}}{\partial \sigma_r} \\ & \cdots & \\ \frac{\partial S_{11,N_m}}{\partial N_p} & \frac{\partial S_{11,N_m}}{\partial r_p} & \frac{\partial S_{11,N_m}}{\partial \sigma_r} \end{pmatrix} \tag{5.4}$$

where $\mathbf{J}$ is also known as *sensitivity matrix* that is comprised of sensitivity coefficients. In the case of nonlinear inverse problems, the solution of Equation 5.3 is obtained with an iterative procedure that results from a Taylor series expansion of $\mathbf{S_{11}}(\mathbf{P})$ around a proposed solution $\mathbf{P}^k$,

$$\mathbf{S_{11}}(\mathbf{P}) = \mathbf{S_{11}}(\mathbf{P}^k) + \mathbf{J}^k\left(\mathbf{P} - \mathbf{P}^k\right) \tag{5.5}$$

where the superscript k denotes the number of iteration. Considering that the exact solution of $\mathbf{S_{11}}(\mathbf{P})$ is represented by the measurements $\mathbf{S_{11}^*}$, and substituting Equation 5.5 into Equation 5.3 to have an iterative procedure to obtain an improved solution for the unknown parameter $\mathbf{P}^{k+1}$ yields,

$$\mathbf{P}^{k+1} = \mathbf{P}^k + \left[\left(\mathbf{J}^k\right)^T\left(\mathbf{J}^k\right)\right]^{-1}\left(\mathbf{J}^k\right)\left[\mathbf{S_{11}}^* - \mathbf{S_{11}}(\mathbf{P}^k)\right] \tag{5.6}$$

where $\left(\mathbf{J}^k\right)^T\left(\mathbf{J}^k\right)$ replaces the Hessian matrix that is used for the Newton-Gauss method. The solution is straight-forward if the approximated Hessian is well-conditioned and is not singular. However, for inverse problems this is not usually the case as inverse problems are known to be ill-posed and for a discretized system, the resulting linear system is usually ill-conditioned. The LM algorithm overcomes this difficulty by modifying the approximated Hessian with an iterative procedure of the following form.

$$\mathbf{P}^{k+1} = \mathbf{P}^k + \left[\left(\mathbf{J}^k\right)^T\left(\mathbf{J}^k\right) + \mu^k\mathbf{\Omega}^k\right]^{-1}\left(\mathbf{J}^k\right)\left[\mathbf{S_{11}}^* - \mathbf{S_{11}}(\mathbf{P}^k)\right] \tag{5.7}$$

where μ is the damping parameter, $\mathbf{\Omega}$ is a diagonal matrix comprised of diagonal elements of $\left(\mathbf{J}^k\right)^T\left(\mathbf{J}^k\right)$.

The following criteria were used to stop the iterative procedure,

$$F(\mathbf{P}^{k+1}) < \epsilon_1 \tag{5.8}$$

$$|\mathbf{P}^{k+1} - \mathbf{P}^k| < \epsilon_2 \tag{5.9}$$

where ϵ_1 and ϵ_2 are the defined tolerances. In this study, ϵ_2 is taken as 10^{-3}, whereas ϵ_1 is calculated based on,

$$\epsilon_1^2 = \int_{-\infty}^{+\infty} x^2 \frac{1}{\sigma\sqrt{2\pi}} \exp\left(\frac{-x^2}{2\sigma^2}\right) N_m dx = N_m\sigma^2 \tag{5.10}$$

where the integral in Equation 5.10. includes all the possible values of the error.

Given synthetic measurement $\mathbf{S_{11}}^*$, initial $\mathbf{P}^0$ and μ^0, the computational algorithm to solve the Equation 5.7 is given below in [73]. In this work, the initial guess for $\mathbf{P}$ is determined randomly within the domain of unknowns and μ^0 is taken as 0.001 as suggested in [73].

5.2.3. Tabu Search (TS) Algorithm

While gradient based methods such as LM algorithm converges fast to a minimum, the converged solution could be a local minimum rather than the global for problems with multiple extrema. For such problems, use of stochastic global search algorithms is essential. Tabu Search (TS), originally proposed by Glover [74], is a meta-heuristic method, developed to solve combinatorial optimization problems such as the traveling salesman. The basic idea in the TS is to take a set of parameters and search the neighborhood of the current point. After searching the neighborhood, the neighboring point which gives the best objective will be taken as the new point to generate new neighbors. At every step, previously visited points are added to a tabu list to avoid coming back to those points again. These two features help TS escape from the local minima.

Although TS algorithm is originally designed to solve combinatorial optimization problems, not all the problems are combinatorial. The simple idea of TS is extended into Continuous Tabu Search (CTS) algorithm by Siarry and Berthiau [75] to solve the problems which has continuous domain. The main difference between two algorithm lies in the definition of neighborhood. Siarry and Berthiau adopt the concept of a ball for the neighborhood and define $B(s, r_n)$ to be a sphere centered at a point s with a radius r_n. Then, the sub-domain $B(s, r_t)$ is partitioned into N_n concentric spheres with user defined radii. Finally, the neighboring points, $s^{'}$, are selected within these concentric spheres. The detailed explanation of the method can be found in [75].

The CTS algorithm is further expanded into Enhanced Continuous Tabu Search (ECTS) method by Chelouah and Siarry [76]. ECTS algorithm contains five stages: Setting of the parameters, diversification, search for the most promising area, inten-

sification and the identification of the best point found. The first and the last stage are fairly straightforward. The aim of the diversification phase is to make sure that the whole domain is searched. While searching the whole domain, diversification phase detects some areas that might contain the global extrema and saves these areas into a promising list for further research. Search for the most promising area takes the promising list and finds the best among them. Finally, intensification phase takes the most promising area and search that area further. In practice, diversification and the intensification phases are very similar to each other. The only differences are the value for the radius of the ball, $B(s, r_n)$, and the definition of the search domain. In this study, the ECTS algorithm presented in [76] is used.

Note that in all algorithms the user defined parameters have significant effect on the solution efficiency. In this study, the search domain is limited to a square area defined by $N_p = [3\ 45]$ and $r_p = [3\ 45]$ nm. However, the search domain can be easily extended to a larger area. The solution domain is first normalized so that the normalized domain is defined as $\bar{N_p} = [0\ 1]$ and $\bar{r_p} = [0\ 1]$. The size of the tabu list and the promising list, l_{tabu} and $l_{promising}$, are set to 400 and 10, respectively. The radius, r_n, which defines the size of the sub-domain is set to 0.3 for the diversification phase as it is observed that larger r_n results in better diversification. In the intensification phase, this value is halved at every step to have finer search. In all phases, the sub-domain is divided into $N_n = 20$ uniformly spaced concentric spheres and $N_n = 20$ neighbors are selected randomly within the domain. The last parameters defining the radius of the tabu and the promising regions are r_t and r_{ps}. If a point is labeled as tabu, the region centered by the point with $r_t = 0.01$ is also added to the tabu list. Similarly, if a point is labeled as promising, the region centered by the point with $r_{ps} = 0.02$ is added to the promising list. Finally, the diversification phase terminates when the maximum number of iterations, $I_{max} = 100$, is reached or the solution satisfies the criterion presented in Equation 5.10 for the Methods 2 and 4. $I_{max} = 500$ is used for Method 6, as this method utilizes the database and computational time is no longer a problem.

5.3. Solution Methodology

In order to understand the feasibility of all possible solution approaches, 4 different methods have been devised based on combination of different alternatives as summarized in Table 5.2. The considered combinations include solution of direct problem (DP) vs using database (DB), and using Levenberg-Marquardt (LM) vs Tabu Search algorithm (TS). It should be noted that orientation averaged results are used in all methods. Finally, Case 8 will be evaluated with the method having the best performance after a rigorous analysis is carried out for monodisperse cases.

Table 5.2. The summary of different models and solvers used in this chapter.

Methods	**Model**	**Solver**
Method 1	DP	LM
Method 2	DP	TS
Method 3	DB	LM
Method 4	DB	TS

5.4. Sensitivity Analysis of S_{11}

Although DDSCAT is a widely used open source code and it was validated numerous times [77, 78], a verification study was carried out at the beginning of this study by reproducing the results presented in [79] to accurately select the parameters of DDSCAT since they affect both the quality of the simulation and the computational time. After required parameters are studied carefully a sensitivity analysis of S_{11} is carried out.

First, the effects of nanoparticle radius, r_p, the number of nanoparticles forming the aggregate, N_p, and the wavelength of the incident light, λ, on the S_{11} are investigated. The wavelengths investigated are chosen based on those used in experimental studies, where the most encountered wavelengths are 266 nm, 532 nm, 798 nm, and

1064 nm [59, 80]. The nanoparticle radii are considered from 15 nm to 60 nm with 15 nm increment, whereas number of nanoparticles are considered from 25 to 100 with 25 increment. These dependencies are investigated by averaging the results of 10 different aggregates and presenting the common logarithm of S_{11}.

Figure 5.1 shows the effect of wavelength on scattering behavior for $N_p = 25$ with different sized particles. It can be observed that the S_{11} values tend to decrease, independent of the nanoparticle radius, as the wavelength increases. The similar observation is valid for $N_p = 50$, 75 and 100. It is observed that reliable characterization below 15 nm for an aggregate of 25 nanoparticles may not be possible since both the S_{11} and measurement uncertainty are in the same order of magnitude, 10^{-4}, at $\lambda = 1064$ nm. This observation is crucial for characterization of aggregates with small nanoparticle radius since the order of magnitude of S_{11} will be comparable with the measurement uncertainty if longer wavelengths are used. Therefore, working with shorter wavelengths would be more informative in such cases and $\lambda = 266$ nm is used in in this study.

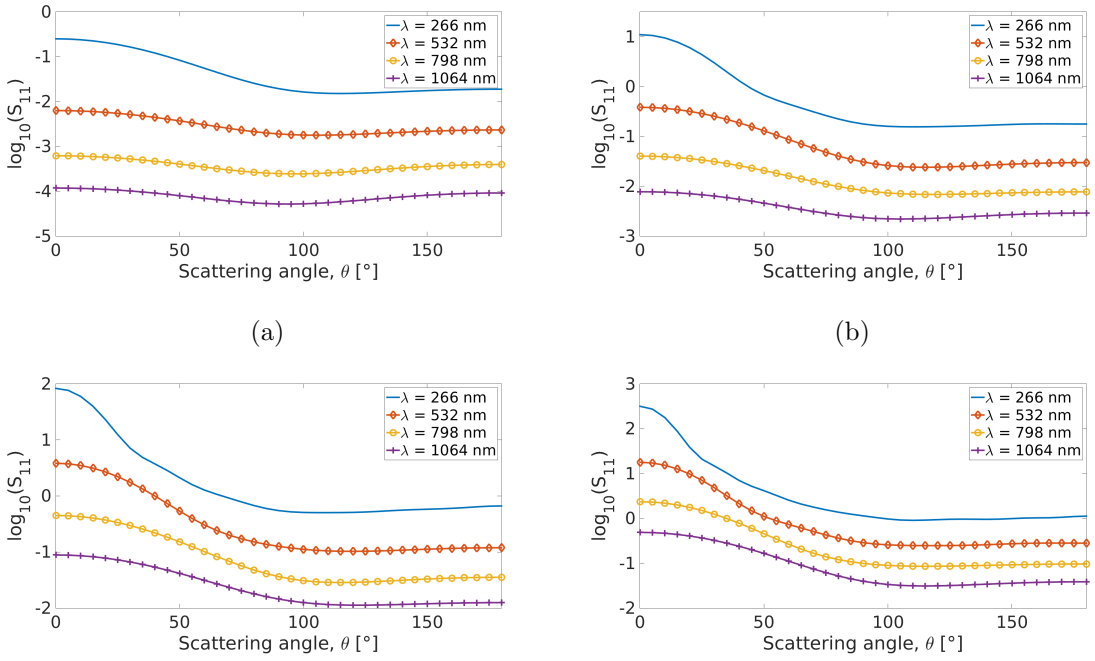

Figure 5.1. The effect of wavelength for aggregates of different sized particles, a) $r_p = 15$ nm, b) $r_p = 30$ nm, c) $r_p = 45$ nm and d) $r_p = 60$ nm, with $N_p = 25$.

Figure 5.2 presents the effect of number of nanoparticles in the aggregate on S_{11}, for $\lambda = 266$ nm. There is approximately one order of magnitude difference between the S_{11} values of $N_p = 25$ and $N_p = 25$ for each particle size considered. The effect of nanoparticle radius on S_{11} at $\lambda = 266$ nm can be observed in Figure 5.3. The Figures 5.2 and 5.3 exhibit similar behavior except that the order of magnitude difference between the S_{11} values of $r_p = 15$ nm and $r_p = 60$ nm are larger in Figure 5.3.

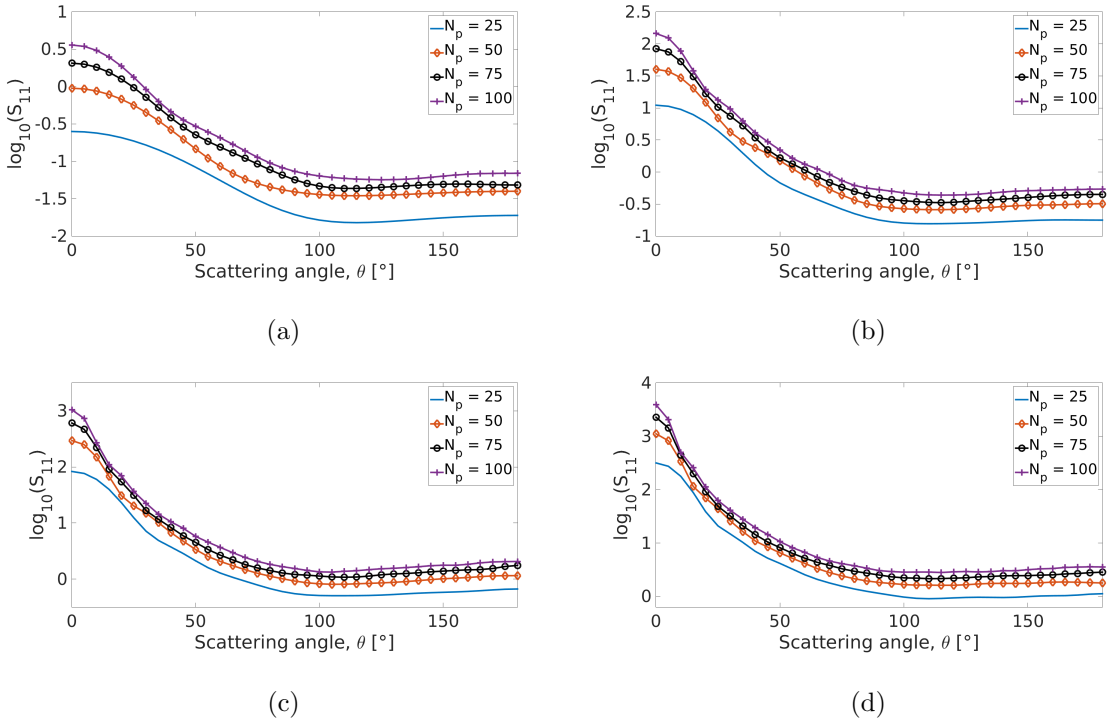

Figure 5.2. The effect of number of nanoparticles forming the aggregate for different sized particles, a) $r_p = 15$ nm, b) $r_p = 30$ nm, c) $r_p = 45$ nm and d) $r_p = 60$ nm, with $\lambda = 266$ nm.

The analysis shows that S_{11} can be used for characterization purposes. However, there are important limitations. First of all, the choice of the wavelength is critical as it has a strong effect on the order of magnitude of the measurements, especially for aggregates formed by smaller sized particles. Secondly, the measurement uncertainty of the experimental device should be as small as possible to obtain reliable measurements. The order of magnitude of the S_{11} tends to decrease as r_p decreases for a given wavelength. Therefore, there exists a lower limit for reliable characterization that will be addressed in the upcoming sections.

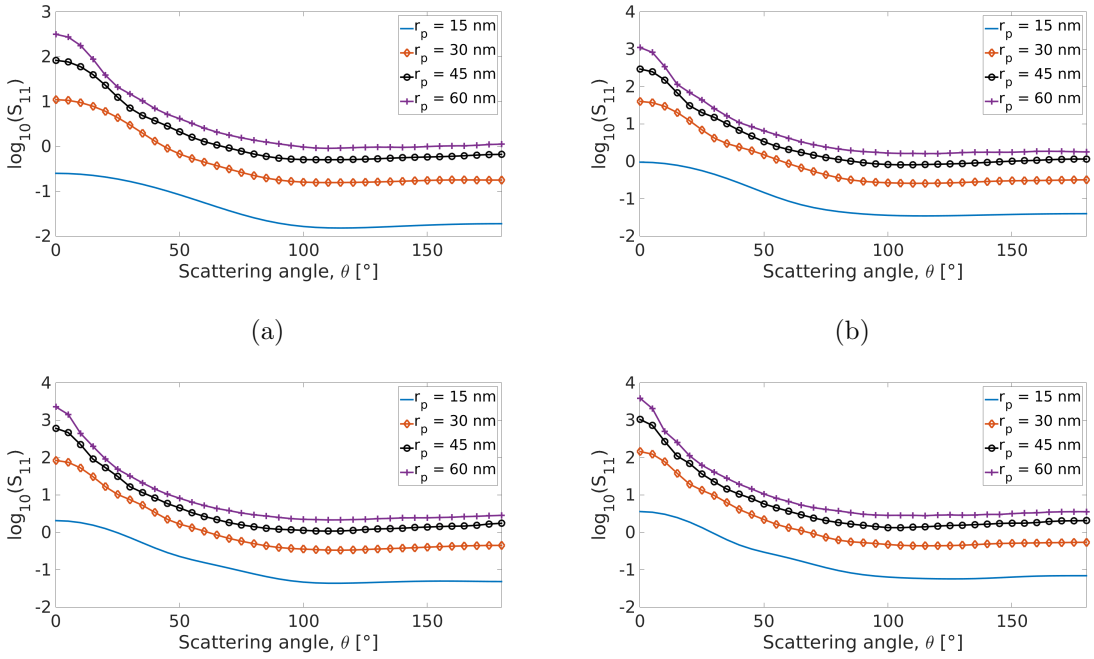

Figure 5.3. The effect of nanoparticle radius forming the aggregate, a) $N_p = 25$, b) $N_p = 50$, c) $N_p = 75$ and d) $N_p = 100$ with $\lambda = 266$ nm.

5.5. Evaluation of Methods

The computational times required by the methods considered here differ significantly. Since Methods 1 and 2 presented in Table 5.2, require high computational time a single random error is introduced to the scattering behavior of each monodisperse aggregate, by considering $j = 1$ in Equation 4.2 for these methods. Therefore, only 10 different synthetic measurement data sets (relying on 10 aggregates, and using a single random error set) are created for evaluation of these methods. Whereas, 100 different synthetic measurement data sets (relying on 10 aggregates, and using 10 random error sets) are utilized for evaluation of Methods 3 and 4 that do not require high computational time like others.

The evaluation of methods are carried out in two steps: First, the performance of the methods summarized in Table 5.2 are tested rigorously using the Case 1 presented in Table 5.1. In the second step, the results of methods are then presented for the remaining 6 cases, Cases 2-7. The polydisperse case will be presented separately.

5.5.1. Case 1

The objective function contour and the objective function variation along r_{eff} = 86.1 nm line are presented for Case 1 in Figure 5.4. The data presented in Figure 5.4 is generated by solving direct problem with orientation averaging. It can be observed that the topology has multiple local minima, and it can be foreseen that the LM algorithm might converge to a local minima based on the initial guess. The objective function along the r_{eff} = 86.1 nm line also confirms this observation, clearly displaying the existence of local minima.

All methods presented in Table 5.2 are applied for Case 1 and the results are presented in Figure 5.5. As can be observed from Figure 5.5, the results estimated by the methods relying on LM (Methods 1 and 3), have high variance. The resulting standard deviations of Methods 1 and 3 for r_p are 2 nm and 5 nm; whereas those for N_p are 8 and 13, respectively. However, the results found by the methods with TS have relatively smaller variance. The resulting standard deviations of Methods 2 and 4 for r_p are 0.7 nm and 0.5 nm; whereas those for N_p are 1 and 0.7, respectively. In summary, the methods relying on LM yield higher standard deviation as they converge to a different local minima in each trial with different initial guesses. The results of both r_p and N_p showed that the Methods 2 and 4 have higher accuracy with relatively small variance in estimating the unknown parameters.

Table 5.3 shows the number of objective function evaluations and computational time required to converge a solution for each method for Case 1 considering different sets of synthetic data used. It can be clearly observed that the methods relying on LM algorithm require less objective function evaluations and computational time than methods relying on TS. However, since methods relying on LM, have lower prediction accuracy with higher uncertainty, use of these methods are not recommended for characterization. The computational time and iterations of the other cases are similar to the values presented in Table 5.3. Therefore, they will not be presented.

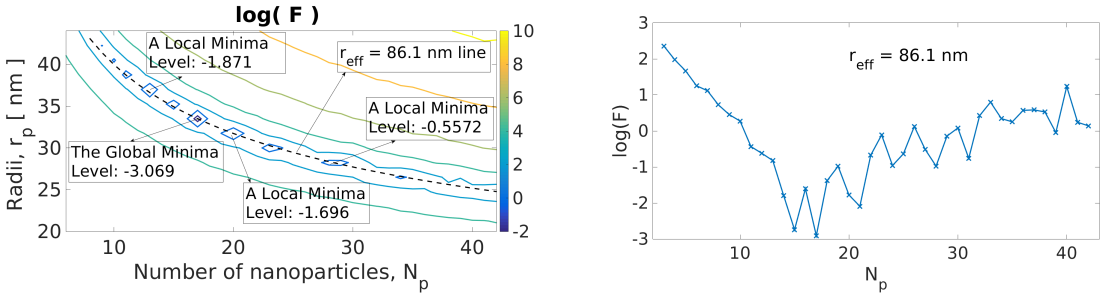

(a) (b)

Figure 5.4. a) Natural logarithm of the objective function of Case 1 and b) objective function along $r_{eff} = 86.1$ nm curve.

Table 5.3. The results of the Case 1 for all methods.

Case 1	**Number of Objective Function Evaluations**	**Time [sec]**
Method 1	36 ± 12	16363 ± 5085
Method 2	1218 ± 274	723782 ± 143340
Method 3	105 ± 62	1 ± 0.7
Method 4	11937 ± 2989	151 ± 38

It was stated earlier that there exists a randomness in the aggregate generation algorithm, and two aggregates that are generated based on same set of parameters have different aggregate geometries. Moreover, the scattering pattern of aggregates that are generated with different but similar set of parameters might be indistinguishable, identifying a uniqueness problem that limits the precision of the method. Three different parameters sets having the same r_{eff} value, $\mathbf{P} = [13\ 36.6\,\text{nm}\ 0]$, $\mathbf{P} = [17\ 33.5\,\text{nm}\ 0]$ and $\mathbf{P} = [23\ 30.3\,\text{nm}\ 0]$, are considered to further investigate the uniqueness problem. 10 different fractal geometries that are created for each parameters sets have different geometries due to the randomness of algorithm used to create aggregates as explained earlier. The forward problem is solved for each 10 fractals sets and the scattering behaviors are estimated. Then, the average scattering profiles and standard deviations of S_{11} values at every scattering angle θ are calculated. The shaded areas in Figure 5.6 show the mean $\pm$ standard deviation calculated for each parameter set. Figure 5.6

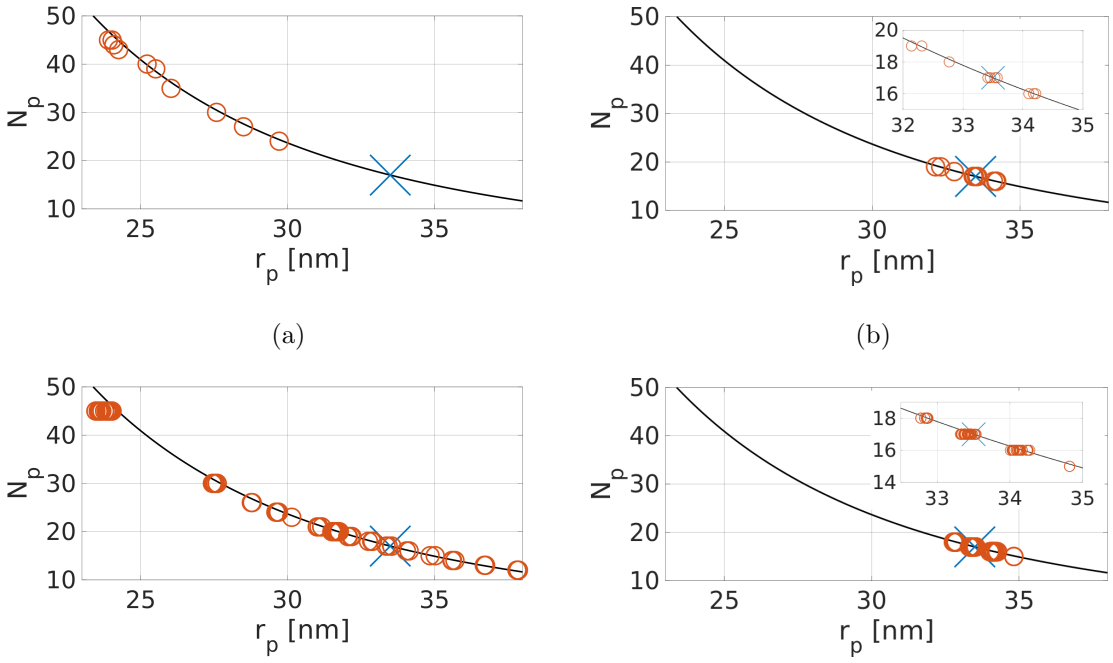

(a) (b)

(c) (d)

Figure 5.5. The results of Case 1 ($N_p = 17$, $r_p = 33.5$ nm) for Methods a) 1, b) 2, c) 3 and d) 4, respectively. The blue cross represents the values of Case 1, and the red circles are the predictions. The solid line represents the $r_{eff} = 86.1$ nm curve.

suggests that the range of S_{11} values covered by each parameters sets overlap with each other, especially for the larger polar angles, highlighting the uniqueness problem that limits the precision of the methods proposed.

5.5.2. Case 2-7

The methods considered are then tested for Cases 2-7 and a summary of the results for all monodisperse cases, based on all the methods are presented in Tables 5.4 and 5.5, respectively. Moreover, the predictions for Cases 2-5 are also presented in Figures 5.7-5.10. The order of magnitude of S_{11} for Cases 6 and 7 are comparable with the sensitivity of measurement device, and the synthetic measurements for these cases are dominated by measurement error. Therefore, their results show high deviation causing large errors and will not be presented here explicitly.

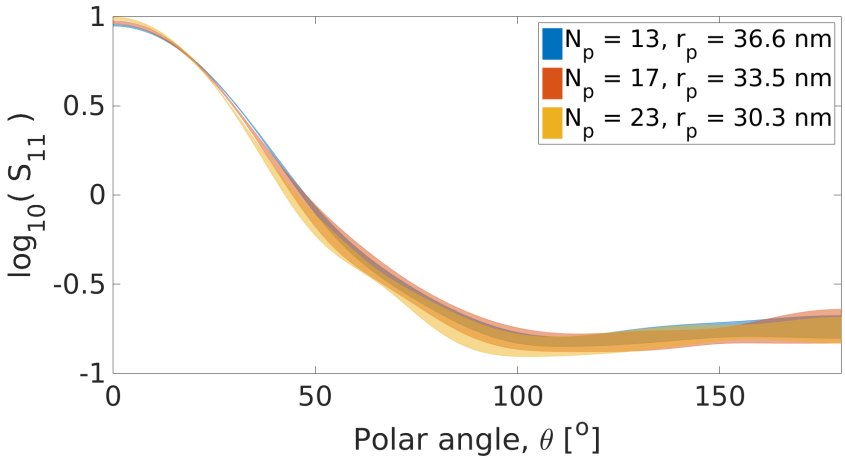

Figure 5.6. Uniqueness problem for Case 1.

It can be observed from Tables 5.4 and 5.5, and Figures 5.7-5.10 that the methods with LM (Methods 1 and 3) fail to consistently converge to the global minimum that represents the correct solution. They converge to different solutions resulting in high prediction uncertainty for radius and number of particles. For the methods relying on TS, Method 2 converges to an acceptable solution in all the cases considered, but it is significantly more computationally expensive. The Method 4 that relies on the database appears to be the most robust, consistent, efficient method with acceptable prediction accuracy. Therefore, using a database with spline fitting can be coupled with the TS algorithm to estimate N_p and r_p of the monodisperse nanoparticle aggregates.

5.5.3. Limitations of the Method

The limits of a reliable characterization depend on the order of magnitude of S_{11} in comparison to the measurement uncertainty that relies on wavelength of the incident light and aggregate size. As mentioned earlier, the wavelength of the incident light is selected accordingly as 266 nm. Figure 5.11 shows the variation in percentage error for predicted r_p and N_p with effective radius, for Method 4 considering all monodisperse cases, for different measurement sensitivity values, σ. It is observed that the prediction errors of both r_p and N_p tend to decrease as r_{eff} increases; whereas, higher errors are observed for N_p in general. Moreover, errors corresponding to Cases 6 and 7

Table 5.4. Mean and standard deviation in estimated nanoparticle radius, r_p, for monodisperse cases.

	Method 1	**Method 2**	**Method 3**	**Method 4**
Case 1	25.9 ± 2.1	33.4 ± 0.7	28.7 ± 4.5	33.6 ± 0.5
Case 2	9.8 ± 2.0	12.1 ± 0.7	10.8 ± 1.4	11.9 ± 0.4
Case 3	15.6 ± 3.1	18.4 ± 0.8	17.0 ± 2.9	18.8 ± 0.6
Case 4	25.5 ± 4.9	26.0 ± 0.9	24.2 ± 3.7	26.1 ± 0.7
Case 5	34.7 ± 1.2	40.1 ± 1.1	36.6 ± 3.2	39.7 ± 1.3
Case 6	7.2 ± 1.7	6.5 ± 1.8	7.2 ± 1.4	8.7 ± 1.3
Case 7	6.5 ± 1.8	7.9 ± 1.4	8.2 ± 1.3	9.8 ± 0.6

are higher than the rest as they consider smaller aggregates for which the synthetic measurement data is dominated by the introduced measurement error. Higher accuracy predictions are possible by using higher sensitivity measurement devices. Since the error percentages in N_p is higher than that of r_p it can be concluded from Figure 5.11b that accurate characterization is obtained when $r_{eff} > 27$ nm, $r_{eff} > 20$ nm and $r_{eff} > 18$ nm for $\sigma = 10^{-3}$, $\sigma = 10^{-4}$ and $\sigma = 10^{-5}$, respectively.

5.5.4. Polydisperse Case

It is well known that soot aggregates have a log-normal particle size distribution. While the first 7 cases consider monodisperse aggregates, the final case considers a polydisperse aggregate with a log-normal particle size distribution.

The synthetic measurement for Case 8 is obtained as follows: First, 100 different aggregates with $N_p = 30$ nanoparticles having a log-normal distribution with $r_p = 15$ nm and $\sigma_r = 1.25$ are created. After the scattering behavior of these aggregates are obtained, a random measurement error is added to each of them. Then, all of these simulated measurements are averaged to represent the scattering behavior of the

Table 5.5. Mean and standard deviation in estimated nanoparticle radius, N_p, for monodisperse cases.

	Method 1	**Method 2**	**Method 3**	**Method 4**
Case 1	37.2 ± 7.8	17.2 ± 1.1	29.9 ± 12.6	16.8 ± 0.7
Case 2	19.0 ± 11.1	7.9 ± 1.4	12.5 ± 7.3	8.2 ± 0.9
Case 3	26.3 ± 12.4	13.3 ± 1.7	20.3 ± 11.9	12.4 ± 1.3
Case 4	27.3 ± 11.1	22.2 ± 2.3	30.1 ± 11.7	21.7 ± 1.8
Case 5	42.4 ± 3.9	27.7 ± 2.3	37.1 ± 7.8	28.8 ± 2.4
Case 6	18.5 ± 7.5	19.4 ± 9.5	14.8 ± 7.3	15.1 ± 10.5
Case 7	31.2 ± 12.2	17.8 ± 9.2	15.9 ± 7.4	5.1 ± 4.3

ensemble even though our preliminary analysis showed that 40 aggregates are adequate.

The synthetic measurement generated above is tested with modified Method 4. Since Case 8 includes an additional unknown standard TS algorithm is slightly modified into nested TS algorithm. Nested TS algorithm first samples different N_p values from the neighborhood of the point at hand (outer TS), and then initializes a standard TS algorithm (inner TS) to find the optimum r_p and σ_r values for each N_p . The results of the inner TS algorithm is used in the outer TS algorithm to find best N_p values. The points with the best objective function values are stored, and intensification phase begins as usual. The parameters related to inner TS algorithm are adjusted as $r_t = 0.002$, $r_{pr} = 0.004$, $r_n = 0.5$ and $N_n = 50$ whereas same parameters related to outer TS algorithm are adjusted as $r_t = 0.01$, $r_{pr} = 0.01$, $r_n = 0.5$ and $N_n = 6$. The search domain of σ_r is bounded by $\sigma_r = [1\ 3]$ and normalized like other parameters.

Figure 5.12 shows the results of the Case 8 using nested TS that relies on the database created with monodisperse aggregates. The predicted values are $N_p = 22$, $r_p = 16.4$ nm, $\sigma_r = 1.28$ and $r_{eff} = 50.2$ nm. It can be observed that the predicted probability density is close to actual probability density. While the predicted values for

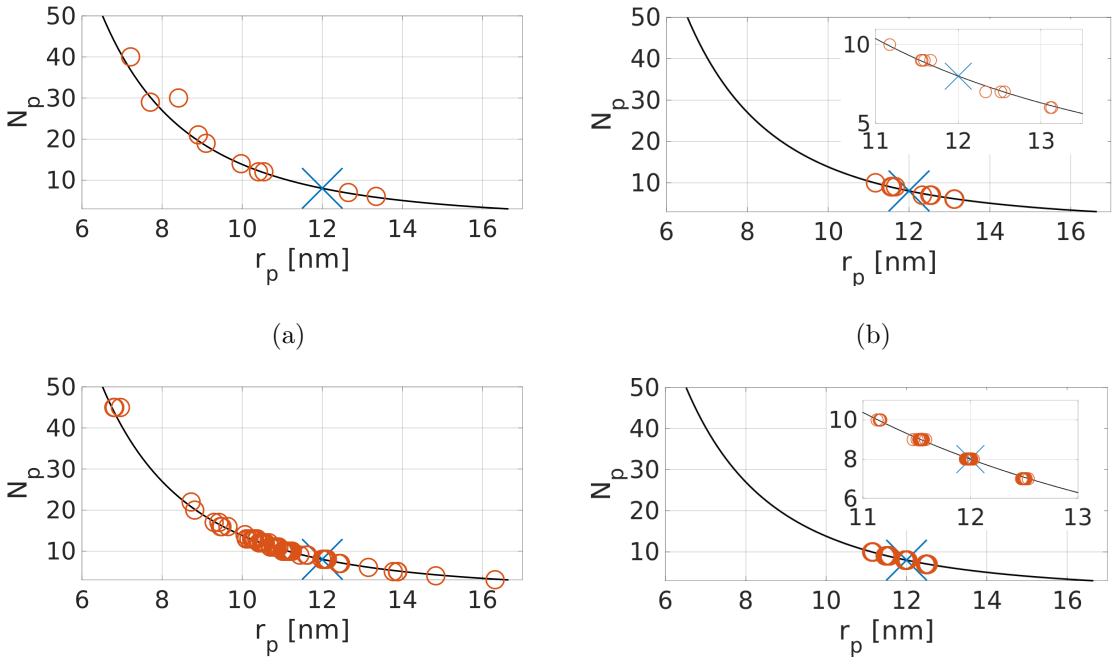

Figure 5.7. The results of Case 2 ($N_p = 8$, $r_p = 12$ nm) for Methods a) 1, b) 2, c) 3 and d) 4, respectively. The blue cross represents the values of Case 2, and the red circles are the predictions. The solid line represents the $r_{eff} = 24$ nm curve.

r_{eff} , r_p and σ_r are reasonably accurate,the predicted N_p value is less than the actual value. The reason for this deviation in N_p might be the particles with small radii are shadowed by particles with large radii.

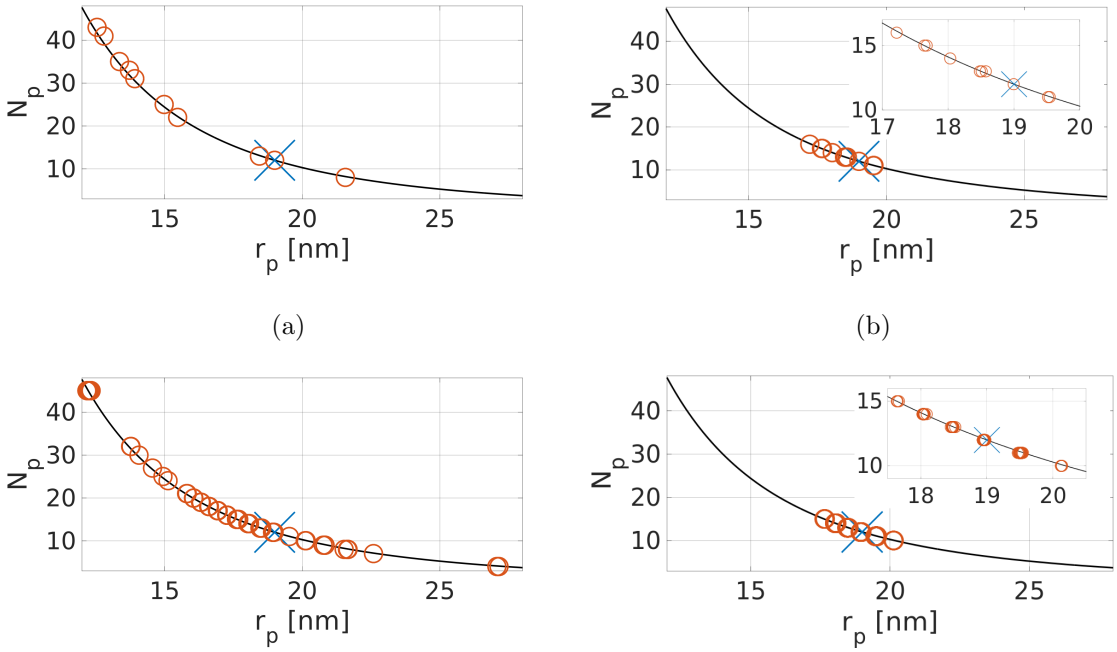

(a) (b)

(c) (d)

Figure 5.8. The results of Case 3 ($N_p = 12$, $r_p = 19$ nm) for Methods a) 1, b) 2, c) 3 and d) 4, respectively. The blue cross represents the values of Case 3, and the red circles are the predictions. The solid line represents the $r_{eff} = 43.5$ nm curve.

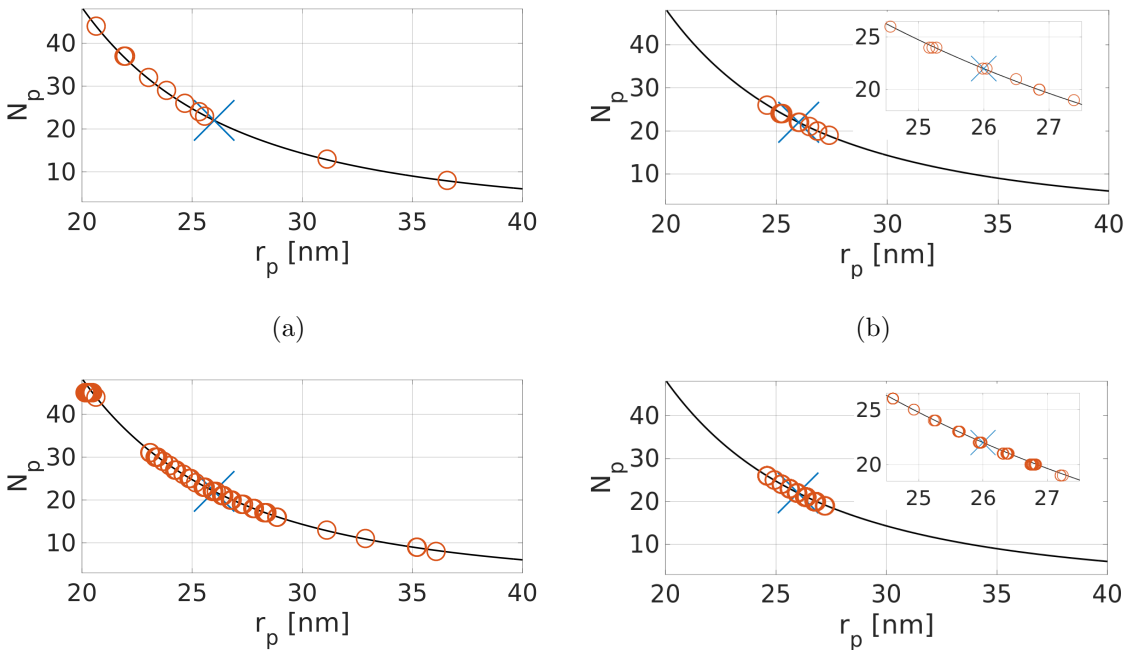

(a) (b)

(c) (d)

Figure 5.9. The results of Case 4 ($N_p = 22$, $r_p = 26$ nm) for Methods a) 1, b) 2, c) 3 and d) 4, respectively. The blue cross represents the values of Case 4, and the red circles are the predictions. The solid line represents the $r_{eff} = 72.8$ nm curve.

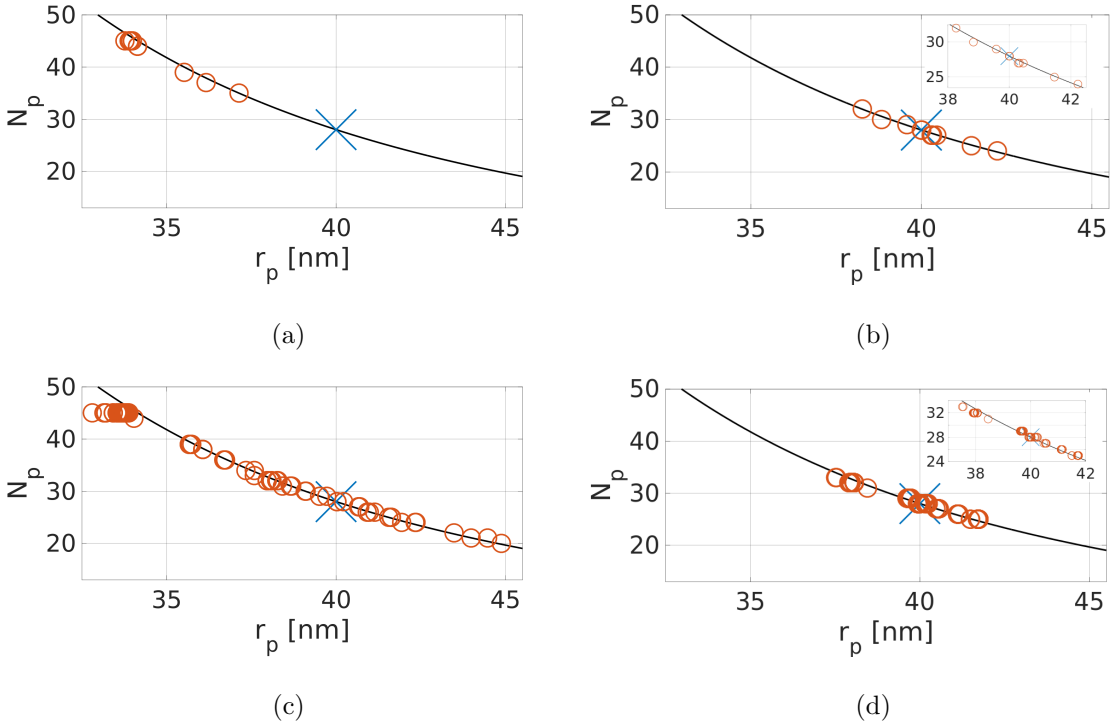

(a) (b)

(c) (d)

Figure 5.10. The results of Case 5 ($N_p = 28$, $r_p = 40$ nm) for Methods a) 1, b) 2, c) 3 and d) 4, respectively. The blue cross represents the values of Case 5, and the red circles are the predictions. The solid line represents the $r_{eff} = 121.5$ nm curve.

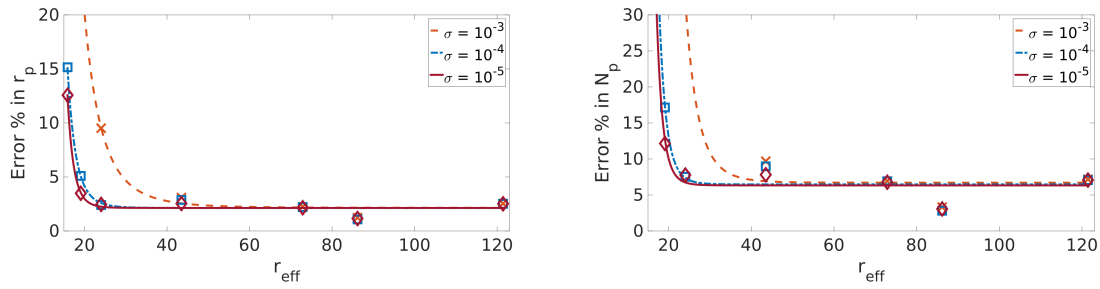

(a) (b)

Figure 5.11. Average error % values (a) in r_p and (b) in N_p for all cases based on for Method 4 for different measurement sensitivity values, σ.

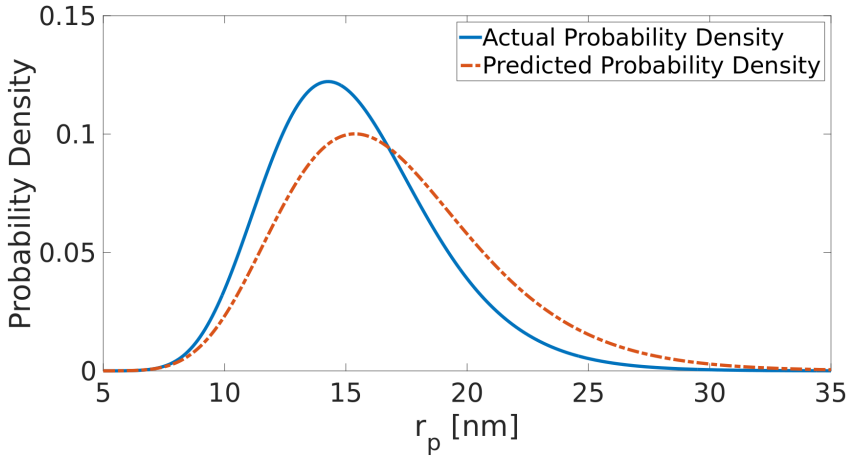

Figure 5.12. The results of Case 8 ($N_p = 30$, $r_p = 15$ nm, $\sigma_r = 1.25$) with nested TS algorithm. The blue curve represents the actual probability density of Case 8, and the red dashed-dot curve represents the probability density based on the predicted values, $N_p = 22$, $r_p = 16.4$ nm, $\sigma_r = 1.28$.

6. CHARACTERIZATION OF NANOPARTICLE AGGREGATES WITH STATISTICAL APPROACHES

In this chapter, characterization of nanoparticle aggregates with statistical approaches is studied. Instead of formulating the inverse problem as a least square minimization problem, all of the parameters of interest are treated as random variables and both standard Bayesian inference methods and Approximate Bayesian Computation (ABC) techniques are applied.

In the case of standard Bayesian inference, the posterior probability distribution is obtained by assuming a likelihood function with a known analytical form; whereas four likelihood-free ABC techniques - Rejection, Markov Chain Monte Carlo, Population Monte Carlo and Adaptive Population Monte Carlo, are used in the case of ABC.

6.1. Bayesian Inference

The very fabric of the statistical inversion is to reconstruct the the solution of the inverse problem in terms of probability distributions. The inverse problems generally comprise of identifying the parameters of interest that are related to the measured quantities through a physical model. Likewise, the statistical inversion theory takes all the information about the system that is known to the observer prior to the measurement as well as the measurement itself and estimates the probability distributions of the parameters of interest. Therefore, the solution of the inverse problem is not a single set of parameters, but a probability distribution referred as the posterior probability distribution. The fundamental principles and some details of the concepts can be found in [81, 82].

In Bayesian statistical inference, all the variables are treated as random variables, which are denoted by capital letters. The observable random variable $S \in R^m$, the measurement, and the unobservable random variable $P \in R^n$, the parameters of

interest, are related to each other by,

$$S = f(P, E) \tag{6.1}$$

where $E \in R^k$ is the noise.

The conditional probability of $\mathbf{P}$ given $S = \mathbf{S_{11}}^*$, $\pi(\mathbf{P}|\mathbf{S_{11}}^*)$, is the solution of the statistical inverse problem as it represents the probability distribution of $P = \mathbf{P}$ based on the measurement $\mathbf{S_{11}}^*$.

$$\pi_{post}(\mathbf{P}) = \pi(\mathbf{P}|\mathbf{S_{11}}^*) = \frac{\pi_{pr}(\mathbf{P})\pi(\mathbf{S_{11}}^*|\mathbf{P})}{\int\limits_{R^n} \pi_{pr}(\mathbf{P})\pi(\mathbf{S_{11}}^*|\mathbf{P})d\mathbf{P}} \tag{6.2}$$

where $\pi_{pr}(\mathbf{P})$ is the prior density that contains all the knowledge about $\mathbf{P}$ before the measurement. The conditional probability of random variable $\mathbf{S_{11}}^*$ given $P = \mathbf{P}$, $\pi(\mathbf{S_{11}}|\mathbf{P})$, is called the likelihood function.

6.1.1. Likelihood Function

Likelihood function is the key to obtain posterior probability distribution of the parameters of interest. As explained briefly in Introduction, there are three ways to compute the likelihood function. In this section, second method which requires the assumption of an analytical likelihood function is adopted as in [40–46].

Notice that additive noise is used in Equation 4.2 and the randomness is eliminated with the database. Fixing $P = \mathbf{P}$ and assuming mutually independent and additive noise make $\mathbf{S_{11}}^*$ conditioned on $P = \mathbf{P}$ to have the same probability density like $\mathbf{E}$, which has a Gaussian distribution.

$$\pi\left(\mathbf{S_{11}}^*|\mathbf{P}\right) = \pi_{noise}\left(\mathbf{S_{11}}^* - g(\mathbf{P})\right) \propto \exp\left(-\frac{1}{\sigma^2}\|\mathbf{S_{11}}^* - g(\mathbf{P})\|\right) \tag{6.3}$$

Finally, the posterior distribution with the assumption of the uniform prior density can be found through calculation and normalization of Equation 6.3.

6.1.2. Test Cases

The cases considered in this section are selected to identify the strengths and the limitations of the method considering the physical limitations explained in Section 4.1, and they are presented in Table 6.1. The cases considered have effective radius ranging between 6.3 nm to 34.9 nm.

Table 6.1. The cases studied for classical Bayesian inference method.

Cases	**Number of particles** N_p	**Mean particle radius** r_p [nm]	**Deviation** σ_r	**Effective radius** r_{eff} [nm]
Case 1	4	10	0	15.8
Case 2	4	4	0	6.3
Case 3	4	22	0	34.9
Case 4	10	4	0	8.6
Case 5	10	16	0	34.5
Case 6	16	4	0	10.1
Case 7	22	10	0	28.0
Case 8	34	10	0	32.4

6.1.3. Results and Discussion

Ten different synthetic measurements are generated for each case presented in Table 6.1. While the analysis carried out for the Case 1 is presented in details to demonstrate the methodology, the results of the other cases that are analyzed following the same procedure is presented without the intermediate steps. All cases are

investigated considering the unscaled posterior distribution that is calculated at discrete points. While the number of nanoparticles is considered from 3 to 45 with an increment of 1, radius of nanoparticles is considered from 3 nm to 45 nm with 0.5 nm increment in the calculations. All the test cases are analyzed relying on measurements with random measurement error introduced. Finally, all of the results are presented by averaging the results of 100 synthetic measurements for each case.

6.1.3.1. Case 1. The effect of measurement error is tested using 10 different error sets that is introduced to 10 simulated measurements, resulting a total of 100 unique synthetic measurements for each case.

The posterior distribution contour for Case 1 based on synthetic measurements is presented in Figure 6.1. Figure 6.1 has multiple peaks at different parameters sets. For example, the probabilities of $\mathbf{P} = [4\ 10\,\text{nm}]^T$ and $\mathbf{P} = [3\ 11\,\text{nm}]^T$ are both around 4.3%. Marginalized probability distributions are often used to construct the credibility intervals. Figure 6.2 presents the marginalized posterior distribution of parameters r_p and N_p. The marginalized posterior probability distributions do not have a known analytical form. The most probable values for number of nanoparticles are 3 and 4, whereas that for nanoparticle radius are 10 nm and 11 nm.

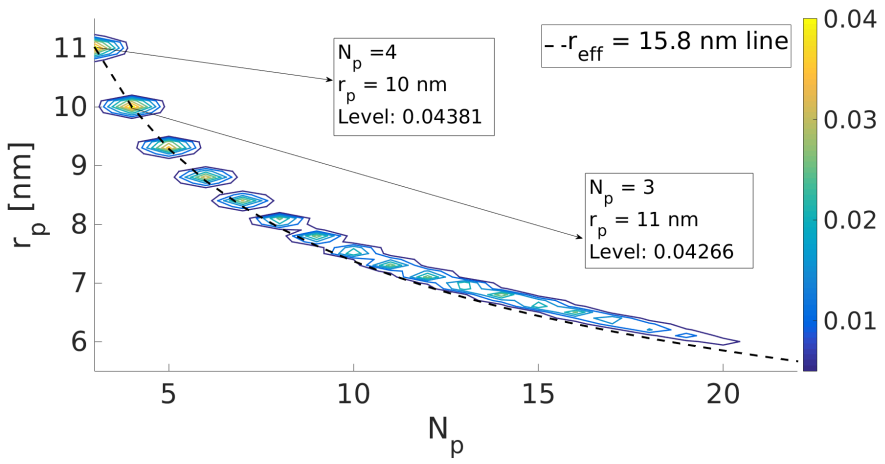

Figure 6.1. Posterior probability distribution of Case 1 ($N_p = 4,\ r_p = 10$ nm).

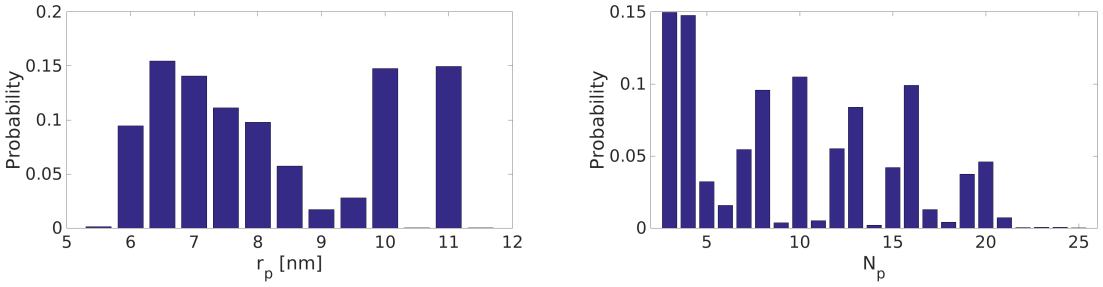

(a) (b)

Figure 6.2. Marginalized posterior probability distribution of parameter a) r_p and b) N_p for Case 1 ($N_p = 4,\ r_p = 10$ nm).

6.1.3.2. Cases 2-8. The remaining cases are also tested with 100 synthetic measurements and the results are presented in Figures 6.3 - 6.9.

Figures 6.2 - 6.9 showed that the posterior probability distributions of both r_p and N_p have large deviation for cases whose effective radius are less than 20 nm (Cases 1, 2, 4 and 6). This observation is consistent with the results presented in Section 5.5.

The results of the cases whose effective radius are larger than 20 nm (Cases 3, 5, 7 and 8) showed that the highest probabilities are associated with either the corresponding true value of the cases or a very similar point near the true value. For example, the predicted values at the maximum probability for Cases 5 and 7 match with the true values presented in Table 6.1. The results predicted for Cases 3 and 8 are within the neighborhood of the corresponding true values. It should be noted that the effective radii of the predicted values and the true values of Case 3 are 34.9 nm and 35.1 nm, respectively. Similarly, that of Cases 8 are 32.5 nm and 32.4 nm.

6.2. Approximate Bayesian Computation

Equation 6.2 suggests that the posterior probability distribution, $\pi_{post}(\mathbf{P})$, can easily be obtained if the analytical forms of both the prior and the likelihood is available. The easiest part in Equation 6.2 is the prior density since it is either known or assumed by the researcher apart from the model. However, representing the likelihood analytically can be impossible for some cases as in most of the computational

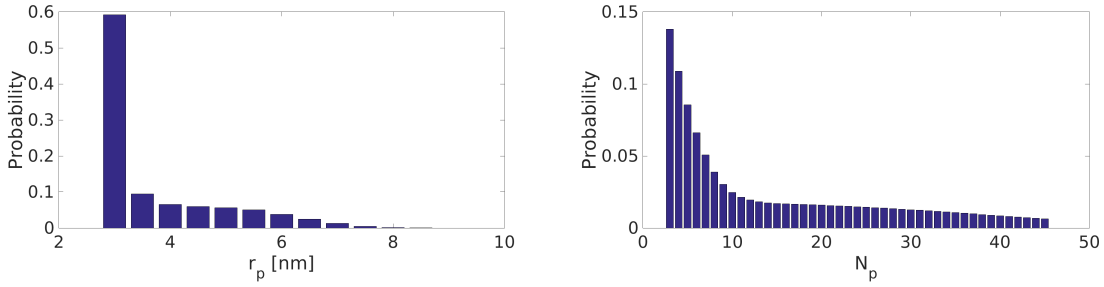

(a) (b)

Figure 6.3. Marginalized posterior probability distribution of parameter a) r_p and b) N_p for Case 2 ($N_p = 4,\ r_p = 4$ nm).

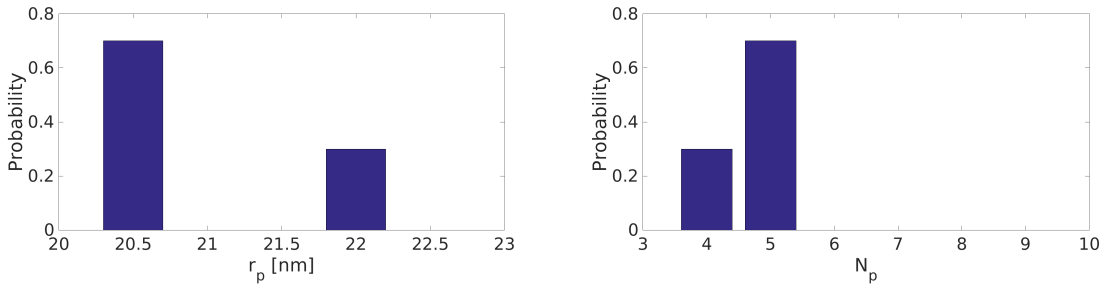

(a) (b)

Figure 6.4. Marginalized posterior probability distribution of parameter a) r_p and b) N_p for Case 3 ($N_p = 4,\ r_p = 22$ nm).

or simulation based models. In these cases, the standard methods of Bayesian estimation can not be applied. As stated earlier, ABC methods overcome this problem by not calculating the likelihood function but sampling enough points from the posterior distribution itself. In this study, four ABC algorithms – Rejection Sampler, Markov Chain Monte Carlo, Population Monte Carlo and Adaptive Population Monte Carlo, are considered.

6.2.1. Rejection Sampler

The first ABC algorithm introduced by Tavaré *et al.* [83] was a simple rejection algorithm to estimate the common ancestor times for DNA sequence data. The idea of Tavaré is extended by Pritchard *et al.* [84]. First, a point, $\mathbf{P}'$, is generated from the prior density. Then, the artificial data set, $\mathbf{S_{11}}(\mathbf{P}')$, associated with the generated point $\mathbf{P}'$ is created using the simulation model, f. They proposed that if the generated

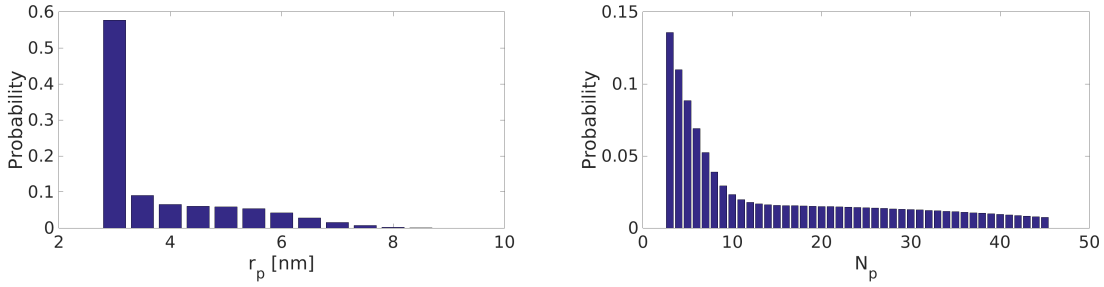

(a) (b)

Figure 6.5. Marginalized posterior probability distribution of parameter a) r_p and b) N_p for Case 4 ($N_p = 10,\ r_p = 4$ nm).

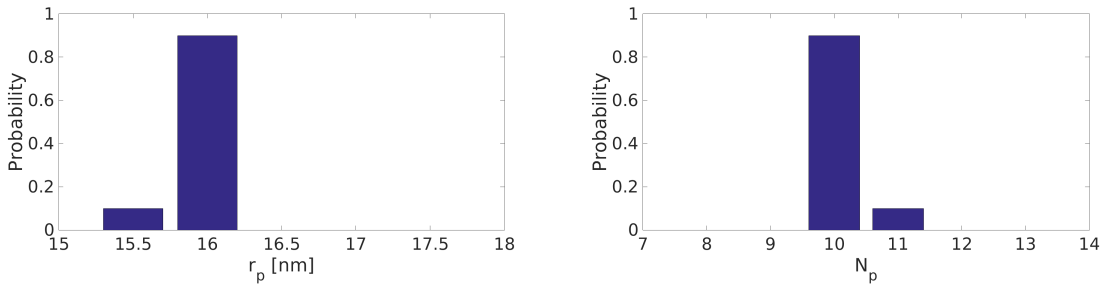

(a) (b)

Figure 6.6. Marginalized posterior probability distribution of parameter a) r_p and b) N_p for Case 5 ($N_p = 10,\ r_p = 16$ nm).

dataset and the actual dataset are close enough, $F(\mathbf{P}') < \epsilon$, then the point is sampled from the posterior. In this inequality, F is a scalar metric and ϵ is the user defined tolerance. If these steps are repeated until N points are drawn from the posterior, a good approximate of the posterior can be obtained without calculating the likelihood function. Algorithm 6.10 presented below is the rejection algorithm proposed by Pritchard. Although it is simple to implement, rejection algorithm suffers from high rejection rates; in other words, low acceptance rates of sampled points.

6.2.2. Markov Chain Monte Carlo (MCMC)

The main disadvantage of the ABC rejection sampler algorithm is the high rejection rates caused by sampling points from the prior distribution. Rejection sampler algorithm samples the new point without using any information from the previously sampled points. However, it is possible, in principle, to reduce the rejection rates by

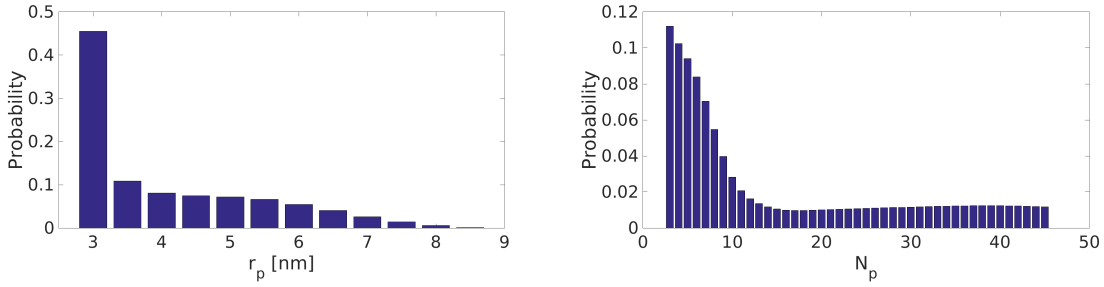

(a) (b)

Figure 6.7. Marginalized posterior probability distribution of parameter a) r_p and b) N_p for Case 6 ($N_p = 16,\ r_p = 4$ nm).

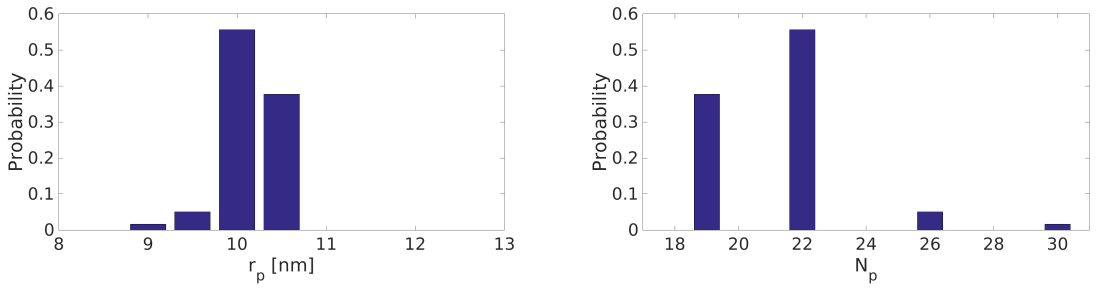

(a) (b)

Figure 6.8. Marginalized posterior probability distribution of parameter a) r_p and b) N_p for Case 7 ($N_p = 22,\ r_p = 10$ nm).

utilizing the information from the previously sampled points. MCMC algorithm samples a new point by making a jump from the current point with the assumption that the new point will possibly be near the last sampled point. Thus, it eliminates the complete randomness and makes use of available information.

MCMC algorithm is similar to the Metropolis-Hasting algorithm. The only difference is that there is no likelihood calculations involved in MCMC. Like Metropolis-Hasting algorithm, MCMC starts with an initial point, $\mathbf{P}^{(0)}$, sampled from the prior. Then, the new points are generated by a transition kernel, q, which relates the point from the previous MC step, $\mathbf{P}^{(i-1)}$, to the new one, $\mathbf{P}'$. Dataset, $\mathbf{S_{11}}(\mathbf{P}')$, is generated by using $\mathbf{P}'$ and $F(\mathbf{P}')$ is calculated. If $F(\mathbf{P}') > \epsilon$, then $\mathbf{P}^{(i-1)}$ is a better approximation than $\mathbf{P}'$, therefore no replacement is made. Otherwise, $\mathbf{P}'$ is accepted with probability, h, where h is a uniformly distributed random number between 0 and 1, $U(0,1)$. It should be noted that MCMC algorithm only uses the last sampled point, not the ones

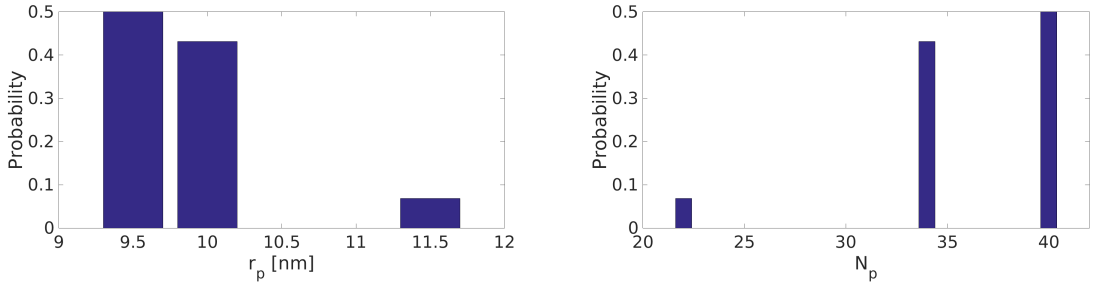

(a) (b)

Figure 6.9. Marginalized posterior probability distribution of parameter a) r_p and b) N_p for Case 8 ($N_p = 34,\ r_p = 10$ nm).

$count = 0$

for $i = 1 \ldots N$ **do**

  while $F(\mathbf{P}^{'}) > \epsilon$ **do**

    $count = count + 1$

    generate $\mathbf{P}^{'} \sim \pi_{pr}(\mathbf{P})$

    simulate $\mathbf{S_{11}}(\mathbf{P}^{'}) \sim f(\mathbf{S_{11}}(\mathbf{P}^{'})|\mathbf{P}^{'})$

  end while

  store $\mathbf{P}_i = \mathbf{P}^{'}$

end for

$r_{accept} = N/count$

Figure 6.10. Rejection Sampler Algorithm.

that are sampled earlier. Algorithm 6.11 given below is the MCMC algorithm proposed by Marjoram *et al.* [85]. More detailed discussions about the algorithm can be found in [86, 87].

Although the acceptance rates of MCMC is higher than the rejection algorithm, there are several disadvantages. First, sampled points are highly correlated to each other due to a transition kernel. This is not a major drawback unless non-correlated points are needed. Second, small ϵ together with high correlation property might cause MCMC to stack in low probability region, resulting in a harder transition from one point to another. Thirdly, covariance matrix should be defined by the user a priori to the algorithm. This has a great impact on the performance of MCMC since covariance

matrix determines the nature of the transition kernel. Finally, it is hard to parallelize MCMC chains [88].

$accepted = 0$
generate $\mathbf{P}^{(0)} \sim \pi_{pr}(\mathbf{P})$
for $i = 1 \ldots N$ **do**
  generate $\mathbf{P}' \sim q(\mathbf{P}'|\mathbf{P}^{(i-1)}, \Sigma)$
  simulate $\mathbf{S_{11}}(\mathbf{P}') \sim f(\mathbf{S_{11}}(\mathbf{P}')|\mathbf{P}')$
  if $F(\mathbf{P}') > \epsilon$ **then**
    $\mathbf{P}^{(i)} = \mathbf{P}^{(i-1)}$
  else
    calculate $h = \frac{\pi_{pr}(\mathbf{P}')}{\pi_{pr}(\mathbf{P}^{(i-1)})} \times \frac{q(\mathbf{P}^{(i-1)}|\mathbf{P}',\Sigma)}{q(\mathbf{P}'|\mathbf{P}^{(i-1)},\Sigma)}$
    if $U(0,1) < h$ **then**
      $accepted = accepted + 1$
      store $\mathbf{P}^{(i)} = \mathbf{P}'$
    else
      store $\mathbf{P}^{(i)} = \mathbf{P}^{(i-1)}$
    end if
  end if
end for
$r_{accept} = accepted/N$

Figure 6.11. Markov Chain Monte Carlo Algorithm.

6.2.3. Population Monte Carlo (PMC)

Using the points that are successfully sampled previously and adjusting the tolerance level ϵ are two good ways to increase the acceptance rate. Partial Rejection Control (PRC) algorithm that Sisson *et al.* [89] proposed uses weighted re-sampling from the points sampled previously and a decreasing tolerance level in each iteration. Beaumont *et al.* [90] corrected the bias noted in the original algorithm proposed by Sisson *et al.* and suggested PMC algorithm. Algorithm 6.12 given below is PMC algorithm suggested by Beaumont *et al.*

PMC divides the calculations into $t = T$ iterations and the corresponding tolerance levels, ϵ_t's, are defined by user with $\epsilon_1 > \epsilon_t > \epsilon_T$. Thus, more points are accepted at the beginning since a relatively relaxed tolerance is applied. The main advantage of PMC is that it samples new points using the points that represent the posterior well, which results in the elimination of the points that represents the posterior poorly.

At $t = 1$, the algorithm samples N points satisfying $F(\mathbf{P}^{'}) < \epsilon_1$ from the prior distribution and assigns a weight, $w_i^{(1)}$, to each of them. Thus, the algorithm has a set of points, $\{\mathbf{P}_i^{(1)}\}_{i=1,2,...N}$, whose elements satisfy the corresponding tolerance level. The set at iteration t, $\{\mathbf{P}_i^{(t)}\}_{i=1,2,...N}$, is formed by selecting a point, $\mathbf{P}_i^{'}$, from the previous set $\{\mathbf{P}_i^{(t-1)}\}_{i=1,2,...N}$ with probability $w_i^{(t-1)}$ and sampling a new point, $\mathbf{P}_i^{(t)}$, by using a transition kernel, $q(\mathbf{P}_i^{(t)}|\mathbf{P}_i^{'}, \Sigma)$. Unlike MCMC, the covariance matrix at each iteration, Σ, is calculated by taking twice the empirical covariance of the set $\{\mathbf{P}_i^{(t-1)}\}_{i=1,2,...N}$.

The major drawback of PMC is the user defined tolerance levels. User may define the tolerances too sharp and too shallow, that leads to an increase or decrease in computation time than required.

6.2.4. Adaptive Population Monte Carlo (APMC)

The problem of user defined tolerances is solved by defining on-line tolerance at each step as suggested by Wegmann *et al.* [91], Drovandi and Pettitt [92] and Del Moral *et al.* [93]. APMC algorithm proposed by Lenormand *et al.* [94] is designed to overcome this problem and based on the basic principles of these works and that of Beaumont *et al.*

APMC takes a step further than PMC by adjusting tolerance levels adaptively. Algorithm 6.13 requires three parameters: N, α and $p_{acc_{min}}$ where N is the total number of points that will be sampled, $\alpha \in [0, 1]$, is the ratio of points that will be kept in each iteration to the total number of points, and $p_{acc_{min}}$ is the minimal acceptance rate. The number of points to keep in each iteration, N_α, is αN.

$count = 0$ and $t = 1$

for $i = 1 \ldots N$ **do**

  while $F(\mathbf{P}_i^{(t)}) < \epsilon_1$ **do**

    $count = count + 1$

    draw $\mathbf{P}_i^{(t)} \sim \pi_{pr}(\mathbf{P})$

    simulate $\mathbf{S_{11}}(\mathbf{P}_i^{(t)}) \sim f(\mathbf{S_{11}}(\mathbf{P}_i^{(t)})|\mathbf{P}_i^{(t)})$

  end while

  let $w_i^{(t)} = 1/N$

end for

let Σ twice the empirical covariance of $\{\mathbf{P}_i^{(t)}\}_{i=1,2,\ldots N}$

for $t = 2 \ldots T$ **do**

  for $i = 1 \ldots N$ **do**

    while $F(\mathbf{P}_i^{(t)}) < \epsilon_t$ **do**

      $count = count + 1$

      pick $\mathbf{P}_i^{'} \sim \mathbf{P}_j^{(t-1)}$ with probabilities $w_j^{(t-1)}$

      sample $\mathbf{P}_i^{(t)} \sim q(\mathbf{P}_i^{(t)}|\mathbf{P}_i^{'}, \Sigma)$

      simulate $\mathbf{S_{11}}(\mathbf{P}_i^{(t)}) \sim f(\mathbf{S_{11}}(\mathbf{P}_i^{(t)})|\mathbf{P}_i^{(t)})$

    end while

    calculate and normalize $w_i^{(t)} \propto \frac{\pi_{pr}(\mathbf{P}_i^{(t)})}{\sum_j w_j^{(t-1)} q(\mathbf{P}_i^{(t)}|\mathbf{P}_j^{(t-1)}, \Sigma)}$

  end for

  let Σ twice the empirical covariance of $\{\mathbf{P}_i^{(t)}\}_{i=1,2,\ldots N}$

end for

$r_{accept} = N/count$

Figure 6.12. ABC Population Monte Carlo Algorithm.

At $t = 1$, the algorithm draws N points from the prior distribution and calculates the $F_i^{(0)}$ and sets $w_i^{(0)} = 1$. Then, the first tolerance level, ϵ_1, is taken as the first α-quantile of $\{F_i^{(0)}\}_{i=1,2,\ldots N}$. After the first tolerance level is determined, APMC constructs the new set, $\{\mathbf{P}_i^{(1)}, w_i^{(1)}, F_i^{(1)}\}$, from the elements of the old set where $F_i^{(0)}$ is smaller than ϵ_1. Thus, a total of N_α elements are obtained at the first iteration. Since the new set consists of the points with the best metrics, $F_i^{(1)}$, the covariance matrix

is taken as twice the empirical covariance of this set. At this point, the rest of the iterations start by setting p_{acc} to 1.

From this point, the algorithm tries to find the best $N - N_\alpha$ points to complete the set at each iteration. At iterations $t > 1$, a new point is generated by drawing a point from the transition kernel, $q(\mathbf{P}_i^{(t-1)}|\mathbf{P}_i', \Sigma)$, around the point $\mathbf{P}_i'$, which is picked from the previous set, $\mathbf{P}_j^{(t-1)}$, with normalized weight (i.e. probabilities), where $j = 1, 2, \ldots N_\alpha$. After the new point is generated the dataset is simulated, and the corresponding metric, and the weight of the old point, $\mathbf{P}_i^{(t-1)}$, and the point itself, are replaced with the new one.

When the process of replacing old points with new ones is finished APMC calculates the new tolerance for the next iteration as the first α-quantile of $\{F_i^{(t-1)}\}_{i=1,2,\ldots N}$ and determines the minimal acceptance rate, p_{acc}. The algorithm repeats these steps until $p_{acc} \leqslant p_{acc_{min}}$.

The main advantage of this algorithm is that the tolerance levels are calculated and updated in each step, resulting in utilization of more optimized tolerance levels.

6.2.5. Metric Function

The main objective of the ABC methods is to sample points from the posterior to approximate the actual posterior distribution of the parameters of interest. This is achieved by defining a metric between the scattering behavior of the actual parameters, $\mathbf{S_{11}}^*$, and that of the simulated parameters, $\mathbf{S_{11}}(\mathbf{P})$.

The ratio of the norm of the difference between $\mathbf{S_{11}}(\mathbf{P})$ and $\mathbf{S_{11}}^*$ to the norm of $\mathbf{S_{11}}^*$ is used as a metric. Since the ABC methods rely on the distance between the simulated estimate, $\mathbf{S_{11}}(\mathbf{P})$, and synthetic measurement, $\mathbf{S_{11}}^*$, a threshold value, ϵ, must be defined to decide whether a point is sampled from the posterior or not. A point is considered to be sampled from the posterior if the metric is smaller than the

$count = 0$ and $N_\alpha = \alpha N$

for $t = 1$ **do**

  for $i = 1 \dots N$ **do**

    $count = count + 1$

    draw $\mathbf{P}_i^{(0)} \sim \pi_{pr}(\mathbf{P})$

    simulate $\mathbf{S_{11}}(\mathbf{P}_i^{(0)}) \sim f(\mathbf{S_{11}}(\mathbf{P}_i^{(0)})|\mathbf{P}_i^{(0)})$

    calculate $F_i^{(0)} = F(\mathbf{P}_i^{(0)})$

    let $w_i^{(0)} = 1$

  end for

  define $\epsilon_1 = Q_{F^{(0)}}(\alpha)$ the first α-quantile of $\{F_i^{(0)}\}_{i=1,2,\dots N}$ and $p_{acc} = 1$

  $\{\mathbf{P}_i^{(1)}, w_i^{(1)}, F_i^{(1)}\} = \{(\mathbf{P}_i^{(0)}, w_i^{(0)}, F_i^{(0)})|F_i^{(0)} \leq \epsilon_1\}_{i=1,2,\dots N}$

  let Σ twice the empirical covariance of $\{\mathbf{P}_i^{(1)}\}_{i=1,2,\dots N_\alpha}$

end for

while $p_{acc} > p_{acc_{min}}$ **do**

  $t = t + 1$

  for $i = N_\alpha + 1 \dots N$ **do**

    $count = count + 1$

    pick $\mathbf{P}'_i \sim \mathbf{P}_j^{(t-1)}$ with probability $\{\overline{w}_j^{(t-1)}\}_{j=1\dots N_\alpha}$

    draw $\mathbf{P}_i^{(t-1)} \sim q(\mathbf{P}_i^{(t-1)}|\mathbf{P}'_i, \Sigma)$

    simulate $\mathbf{S_{11}}(\mathbf{P}_i^{(t-1)})) \sim f(\mathbf{S_{11}}(\mathbf{P}_i^{(t-1)}))|\mathbf{P}_i^{(t-1)})$

    calculate and update $F_i^{(t-1)} = F(\mathbf{P}_i^{(t-1)})$

    update $w_i^{(t-1)} \propto \frac{\pi_{pr}(\mathbf{P}_i^{(t-1)})}{\sum_j w_j^{(t-1)} q(\mathbf{P}_i^{(t-1)}|\mathbf{P}_j^{(t-1)}, \Sigma)} \quad j = 1 \dots N_\alpha$

  end for

  calculate and update $p_{acc} = \frac{1}{N - N_\alpha} \sum_{k=N_\alpha+1}^{N} \mathbf{1}_{F_i^{(t-1)} < \epsilon_{t-1}}$

  let $\epsilon_t = Q_{F^{(t-1)}}(\alpha)$ the first α-quantile of $\{F_i^{(t-1)}\}_{i=1,2,\dots N}$

  $\{\mathbf{P}_i^{(t)}, w_i^{(t)}, F_i^{(t)}\} = \{(\mathbf{P}_i^{(t-1)}, w_i^{(t-1)}, F_i^{(t-1)})|F_i^{(t-1)} \leq \epsilon_t\}_{i=1\dots N}$

  let Σ twice the empirical covariance of $\{\mathbf{P}_i^{(t)}\}_{i=1,2,\dots N_\alpha}$

end while

$r_{accept} = N_\alpha / count$

Figure 6.13. Adaptive Population Monte Carlo Algorithm.

user defined tolerance,

$$F(\mathbf{P}) = \frac{\|\mathbf{S_{11}}(\mathbf{P}) - \mathbf{S_{11}}^*\|}{\|\mathbf{S_{11}}^*\|} < \epsilon \tag{6.4}$$

The definition of the distance metric is same for all the algorithms considered in this work. Secondly, all algorithms assume a uniform prior density, meaning that there is no knowledge about the parameters of interest before the experiments. Choice of uniform prior is common practice in literature [41, 44]. Thirdly, all algorithms except for Algorithm 6.11 sample 100 point from the posterior distribution. Since Algorithm 6.11 is MCMC the number of points that will be sampled can not be controlled with given implementation. Moreover, the transition kernel, q, is assumed as Gaussian with a known covariance matrix for Algorithms 6.11, 6.12 and 6.13. However, some parameters are different from each other for different algorithms.

The covariance matrix is taken as [36 -10; -10 36] for Algorithm 6.11. The covariance matrices in Algorithms 6.12 and 6.13 are calculated empirically based on the previously sampled points. The threshold value is taken as $\epsilon = 0.03$ for Algorithms 6.10 and 6.11 whereas the interval [0.1 0.03] is divided into $T = 9$ equally spaces for Algorithm 6.12 where $T = 9$ is the total number of iterations in Algorithm 6.12. Finally, $\alpha = 0.5$ and $p_{acc_{min}} = 0.01$ are taken as inputs for Algorithm 6.13.

It should be noted that although Algorithms 6.12 and 6.13 have their stopping criteria, covariance matrix may also cause these algorithms to stop. The covariance matrix is symmetric and positive-definite by definiton. If all the sampled points are identical or similar to each other, then, covariance among the sampled points would be equal to or very close to 0. Algorithms 6.12 and 6.13 terminates as the covariance matrix is no more positive-definite and it is assumed that the algorithm converges to that particular point.

6.2.6. Test Cases

The cases considered in this chapter have effective radius ranging between 13 nm to 75 nm. Test cases presented in Table 6.2 are defined considering the observations mentioned in Section 4.1.

Table 6.2. The cases studied for Approximate Bayesian Computation methods.

Cases	**Number of particles** N_p	**Mean particle radius** r_p [nm]	**Deviation** σ_r	**Effective radius** r_{eff} [nm]
Case 1	34	4	0	13
Case 2	4	10	0	16
Case 3	10	10	0	21
Case 4	16	16	0	40
Case 5	34	16	0	52
Case 6	40	22	0	75
Case 7	30	15	1.25	50

6.2.7. Results and Discussion

The results for Case 4, shown in Table 6.2, is presented rigorously first comparing the performance of the four algorithms. Following the identification of the algorithm with the superior performance considering estimation accuracy and efficiency, the selected algorithm is tested for all cases to determine the limits of characterization.

6.2.7.1. Case 4. The ellipsoids are plotted with mean and covariance matrix of the points sampled from the posterior for each algorithm. Figure 6.14 shows the results for Case 4. It can be observed that the sampled points for all algorithms follow the

corresponding constant effective radius curve calculated with Equation 4.1 as expected. APMC algorithm gives the narrowest ellipsoid among others while still capturing the true value.

Figure 6.15 shows the time elapsed to accept a point for all algorithms and the acceptance ratio, which is defined as the ratio of total number of sampled points to the total number of trials. It can be observed that the rejection algorithm has the highest time with lowest acceptance rate as low as 0.03% whereas APMC algorithm has the lowest time with highest acceptance rate of 1.8%. Since APMC algorithm gives accurate results in a reasonable amount of time with high acceptance rates, the other cases are only investigated with APMC method. As the time and acceptance rate results are similar for the other cases they are not presented here explicitly.

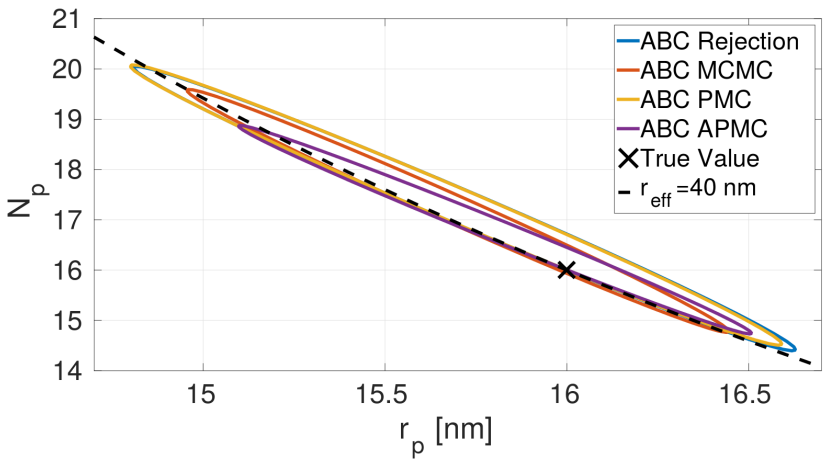

Figure 6.14. The results of Case 4 ($N_p = 16$, $r_p = 16$ nm, $\sigma_r = 0$) for all algorithms.

6.2.7.2. Monodisperse Cases (Cases 1-6). Figure 6.16 shows the results of Cases 1-6 considered. Again, the ellipsoids are plotted with the mean and covariance matrix of the corresponding sampled points. All of the ellipsoids include corresponding true values that are defined in Table 6.2 and are marked with a cross sign. When the effective radius is less than 20 nm, the ellipsoids grow larger and the deviations begin to increase. For the smaller aggregates, the order of magnitude of measurement error becomes comparable to, or larger than the measured S_{11} values. Considering these results, we can safely say that the characterization is reliable above the 20 nm effective

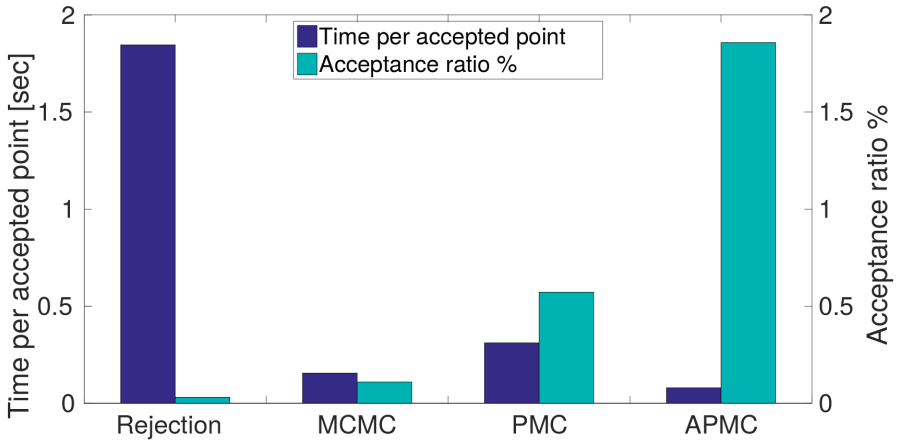

Figure 6.15. Time and acceptance rate of all algorithms for Case 4.

radius curve for 266 nm light source.

Figure 6.16 also suggest that the deviations in r_p is less than 2 nm and that of N_p is around 3-4. Finally, each case follows their constant effective radius curve though not shown here explicitly.

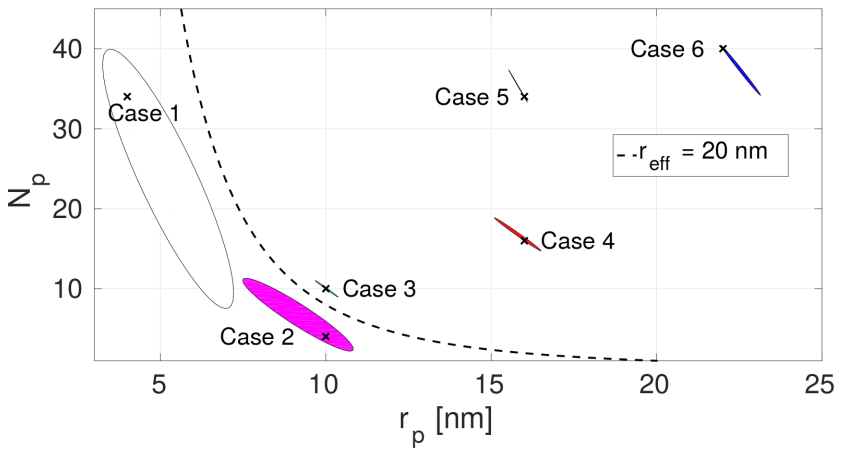

Figure 6.16. The results of all monodisperse cases combined. Cross signs indicate the corresponding true values that are defined in Table 6.2.

6.2.7.3. Polydisperse Case (Case 7). In reality, it is well known that the radii of the soot aggregates follow a log-normal distribution. A preliminary analysis is carried out to understand the applicability of the proposed method for such aggregates. For

that, monodispersity assumption for nanoparticle radii is omitted and an aggregate of $N_p = 30$ particles with a log-normal size distribution with $r_p = 15$ nm and $\sigma = 1.25$, which is typical for soot aggregates [10, 95] is considered for Case 7.

The results plotted in Figure 6.17 are obtained by sampling 1000 points using APMC algorithm with $p_{acc_{min}} = 0.01$. Figure 6.17 shows the probability density values of N_p, r_p and σ_r. It can be observed that the peak probabilities occur near the expected parameters except for N_p. Although the range for results are larger than desired, a rigorous analysis on other S_{ij} profiles along with ABC methods may provide significant improvement on solution accuracy.

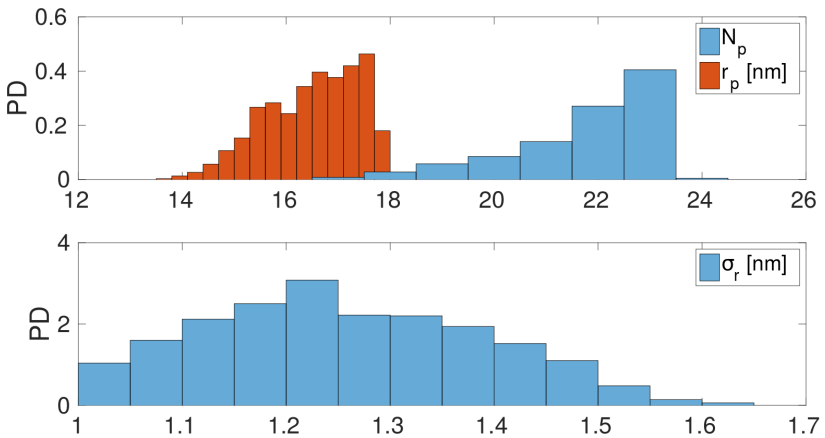

Figure 6.17. APMC results of Case 7 ($N_p = 30$, $r_p = 15$ nm, $\sigma_r = 1.25$ nm). PD stands for probability density values.

7. CONCLUSION

Optical characterization of nanoparticle aggregates via light scattering experiments is investigated via both optimization methods and statistical approaches. The existing state of the art in aggregate characterization with light scattering relies on polarized light experiments and a priori measurements. All of the methods rely on unpolarized light measurements that does not necessitate any prior measurements is proposed and evaluated.

Ensembles of similar and well separated aggregates are considered in this study so that light scattering behavior can be represented by modeling the orientation averaged behavior of a single aggregate using discrete dipole approximation. Filippov's particle cluster algorithm is used to generate the aggregates based on fractal parameters k_f and D_f . While the aggregates generated by the particle-cluster algorithm only approximates the imposed fractal parameters, this resembles a more realistic case. A spline fitted to a database is used for predicting the light scattering behavior of different aggregates as estimation of orientation averaged scattering behavior necessitates significant computation time.

In the first part of this work, the inverse problem is formulated as a nonlinear-least squares minimization problem that is solved using optimization methods. A total of 8 cases are considered in the corresponding chapter. First seven cases assume monodisperse aggregates with particle radius and number range of 10-40 nm, and 4-28, respectively. Whereas, the last case considers a polydisperse aggregate with 30 particles with a log-normal size distribution having a mean particle radius of 15 nm, and a standard deviation of 1.25. It was observed that gradient based techniques such as Levenberg-Marquardt algorithm might converge to erroneous solutions due to the topology with multiple local extrema, and use of global search algorithms is necessary. Therefore, Tabu Search algorithm is applied for the solution of problem.

In the second part of this work, the same problem is considered statistically and the parameters of interest are treated as random variables. Both classical Bayesian inference methods and Approximate Bayesian Computation techniques are used to solve the problem. Total of 8 cases are considered for standard Bayesian inference method and the assumption of additive noise is considered. In the case of ABC, the capability and limitations of four ABC methods; rejection, MCMC, PMC and APMC, are investigated for characterization of both monodisperse and polydisperse soot aggregates based on numerical light scattering measurements. 7 cases with effective radii ranging from 13 nm to 75 nm are considered. It is shown that similar results can be found by all methods investigated. However, APMC algorithm is superior to others in terms of high acceptance rates and low computation time it requires.

It was observed that nanoparticle radius can be found with a deviation less than 2 nm and the number of particles forming the aggregate can be found with a deviation of 3-4 for monodisperse cases. All of the methods predict the number of particles and particle radius confidently, down to an effective radius of 20 nm, without using any polarization information or ex-situ measurement of particle size or number when a 266 nm light source is used. Moreover, promising results are also obtained for the polydisperse case.

It should be noted that the limitations would vary if other wavelengths are considered. Effects of the use of different wavelengths and other Mueller matrix elements on solution sensitivity and limitations should also be investigated. Finally, a more challenging characterization problem briefly investigated here should be examined in more details. For example, the effects of polarization information and distribution parameters on solution accuracy should be investigated. Another distribution for the number of nanoparticles can also be assumed instead of taking a single aggregate. Moreover, necking and overlapping may occur while formation of soot aggregates. A model that takes these parameters into account would be more realistic, and may need to use polarization information stored in other elements of the Mueller matrix.

REFERENCES

1. Jain, P. K., X. Huang, I. H. El-Sayed and M. a. El-Sayed, "Noble metals on the nanoscale: Optical and photothermal properties and some applications in imaging, sensing, biology, and medicine", *Accounts of Chemical Research*, Vol. 41, No. 12, pp. 1578–1586, 2008.

2. Agasti, S. S., S. Rana, M.-H. Park, C. K. Kim, C.-C. You and V. M. Rotello, "Nanoparticles for detection and diagnosis", *Advanced Drug Delivery Reviews*, Vol. 62, No. 3, pp. 316–328, 2010.

3. Litton, C. D. and I. E. Perera, "Modeling the optical properties of combustion-generated fractal aggregates", *Fuel*, Vol. 130, pp. 215–220, 2014.

4. Myung, C. L., A. Ko and S. Park, "Review on characterization of nano-particle emissions and pm morpology from internal combustion engines: part 1", *International Journal of Automotive Technology*, Vol. 15, No. 2, pp. 209–218, 2014.

5. Choi, S., C. L. Myung and S. Park, "Review on characterization of nano-particle emissions and pm morpology from internal combustion engines: part 2", *International Journal of Automotive Technology*, Vol. 15, No. 2, pp. 219–227, 2014.

6. Black, K. C. L., Y. Wang, H. P. Luehmann, X. Cai, W. Xing, B. Pang, Y. Zhao, C. S. Cutler, L. V. Wang, Y. Liu and Y. Xia, "Radioactive 198Au-Doped Nanostructures with Different Shapes for In Vivo Analyses of Their Biodistribution, Tumor Uptake, and Intratumoral Distribution", *ACS Nano*, Vol. 8, No. 5, pp. 4385–4394, 2014.

7. Liati, A., D. Schreiber, P. Dimopoulos Eggenschwiler, Y. Arroyo Rojas Dasilva and A. C. Spiteri, "Electron microscopic characterization of soot particulate matter emitted by modern direct injection gasoline engines", *Combustion and Flame*, Vol. 166, pp. 307–315, 2016.

8. Mukawa, K., N. Oyama, H. Ando, T. Sugiyama, S. Ogo and Y. Sekine, "Synthesis of stable anisotropic carbon particle aggregates covered by surface nano-graphitic sheets", *Carbon*, Vol. 88, pp. 33–41, 2015.

9. Kozan, M., J. Thangala, R. Bogale, M. P. Mengüç and M. K. Sunkara, "In-situ characterization of dispersion stability of WO3 nanoparticles and nanowires", *Journal of Nanoparticle Research*, Vol. 10, No. 4, pp. 599–612, 2008.

10. Daun, K. J., B. J. Stagg, F. Liu, G. J. Smallwood and D. R. Snelling, "Determining aerosol particle size distributions using time-resolved laser-induced incandescence", *Applied Physics B: Lasers and Optics*, Vol. 87, No. 2, pp. 363–372, 2007.

11. Michelsen, H. A., C. Schulz, G. J. Smallwood and S. Will, "Laser-induced incandescence: Particulate diagnostics for combustion, atmospheric, and industrial applications", *Progress in Energy and Combustion Science*, Vol. 51, pp. 2–48, 2015.

12. Kerker, M., *The scattering of light and other electromagnetic radiation*, Vol. 16, Academic Press, New York, 1969.

13. Sorensen, C. M., "Light Scattering by Fractal Aggregates: A Review", *Aerosol Science and Technology*, Vol. 35, No. 2, pp. 648–687, 2001.

14. Faeth, G. M. and Ü. Ö. Köylü, "Soot Morphology and Optical Properties in Non-spreximed Turbulent Flame Environments", *Combustion Science and Technology*, Vol. 108, pp. 207–229, 1995.

15. Farias, T. L., Ü. Ö. Köylü and M. G. Carvalho, "Range of validity of the Rayleigh—Debye—Gans theory for optics of fractal aggregates", *Applied Optics*, Vol. 35, No. 33, pp. 6560–6567, 1996.

16. Kim, J., H. Bauer, T. Dobovičnik, R. Hitzenberger, D. Lottin, D. Ferry and A. Petzold, "Assessing Optical Properties and Refractive Index of Combustion Aerosol Particles Through Combined Experimental and Modeling Studies", *Aerosol Sci-*

ence and Technology, Vol. 49, No. 5, pp. 340–350, 2015.

17. Klusek, C., S. Manickavasagam and M. Mengüç, "Compendium of scattering matrix element profiles for soot agglomerates", *Journal of Quantitative Spectroscopy and Radiative Transfer*, Vol. 79, No. SI, pp. 839–859, 2003.

18. Koylu, U. O. and G. M. Faeth, "Radiative Properties of Flame-Generated Soot", *Journal of Heat Transfer*, Vol. 115, No. 2, pp. 409–417, 1993.

19. Zhao, Y. and L. Ma, "Applicable range of the Rayleigh-Debye-Gans theory for calculating the scattering matrix of soot aggregates", *Applied Optics*, Vol. 48, No. 3, pp. 591–597, 2009.

20. Peterson, B. and S. Ström, "T-matrix for electromagnetic scattering from an arbitrary number of scatterers and representations of E(3)", *Physical Review D*, Vol. 8, No. 10, pp. 3661–3678, 1973.

21. Mishchenko, M. I., J. W. Hovenier and L. D. Travis, *Light scattering by nonspherical particles: theory, measurements and applications*, Academic Press, San Diego, 1999.

22. Liu, L., M. I. Mishchenko and W. Patrick Arnott, "A study of radiative properties of fractal soot aggregates using the superposition T-matrix method", *Journal of Quantitative Spectroscopy and Radiative Transfer*, Vol. 109, No. 15, pp. 2656–2663, 2008.

23. Doner, N. and F. Liu, "Impact of necking and overlapping on radiative properties of coated soot aggregates", *Aerosol Science and Technology*, Vol. 51, No. 4, pp. 532–542, 2017.

24. DeVoe, H., "Optical Properties of Molecular Aggregates. I. Classical Model of Electronic Absorption and Refraction", *The Journal of Chemical Physics*, Vol. 41, No. 2, pp. 393–400, 1964.

25. DeVoe, H., "Optical Properties of Molecular Aggregates. II. Classical Theory of the Refraction, Absorption, and Optical Activity of Solutions and Crystals", *The Journal of Chemical Physics*, Vol. 43, No. 9, pp. 3199–3208, 1965.

26. Purcell, E. M. and C. R. Pennypacker, "Scattering and Absorption of Light by Nonspherical Dielectric Grains", *The Astrophysical Journal*, Vol. 186, No. 2, pp. 705–714, 1973.

27. Draine, B. T., "The discrete-dipole approximation and its application to interstellar graphite grains", *The Astrophysical Journal*, Vol. 333, No. 2, pp. 848–872, 1988.

28. Draine, B. T. and P. J. Flatau, "Discrete-dipole approximation for scattering calculations", *Journal of the Optical Society of America A*, Vol. 11, No. 4, pp. 1491–1499, 1994.

29. Yurkin, M. A., V. P. Maltsev and A. G. Hoekstra, "The discrete dipole approximation for simulation of light scattering by particles much larger than the wavelength", *Journal of Quantitative Spectroscopy and Radiative Transfer*, Vol. 106, No. 1-3, pp. 546–557, 2007.

30. McDonald, J., A. Golden and S. G. Jennings, "Opendda: a Novel High-Performance Computational Framework for the Discrete Dipole Approximation", *International Journal of High Performance Computing Applications*, Vol. 23, No. 1, pp. 42–61, 2009.

31. Talebi Moghaddam, S., H. Ertürk and M. P. Mengüç, "Enhancing local absorption within a gold nano-sphere on a dielectric surface under an AFM probe", *Journal of Quantitative Spectroscopy and Radiative Transfer*, Vol. 178, No. SI, pp. 124–133, 2016.

32. Karlsson, A., T. Yi and P.-E. Bengtsson, "Absorption and scattering of light from ensembles of randomly oriented aggregates", *Journal of the Optical Society of America. A*, Vol. 30, No. 3, pp. 316–24, 2013.

33. Reimann, J., S. A. Kuhlmann and S. Will, "2D aggregate sizing by combining laser-induced incandescence (LII) and elastic light scattering (ELS)", *Applied Physics B: Lasers and Optics*, Vol. 96, No. 4, pp. 583–592, 2009.

34. Huber, F. J. T., M. Altenhoff and S. Will, "A mobile system for a comprehensive online-characterization of nanoparticle aggregates based on wide-angle light scattering and laser-induced incandescence", *Review of Scientific Instruments*, Vol. 87, No. 5, pp. 053102–1–9, 2016.

35. Liu, F., C. Wong, D. R. Snelling and G. J. Smallwood, "Investigation of Absorption and Scattering Properties of Soot Aggregates of Different Fractal Dimension at 532 nm Using RDG and GMM", *Aerosol Science and ...*, Vol. 47, No. 12, pp. 1393–1405, 2013.

36. Huber, F. J. T., S. Will and K. J. Daun, "Sizing aerosolized fractal nanoparticle aggregates through Bayesian analysis of wide-angle light scattering (WALS) data", *Journal of Quantitative Spectroscopy and Radiative Transfer*, Vol. 184, pp. 27–39, 2016.

37. Mengüç, M. and S. Manickavasagam, "Characterization of size and structure of agglomerates and inhomogeneous particles via polarized light", *International Journal of Engineering Science*, Vol. 36, No. 12-14, pp. 1569–1593, 1998.

38. Charnigo, R., M. Francoeur, M. P. Mengüç, A. Brock, M. Leichter and C. Srinivasan, "Derivatives of scattering profiles: tools for nanoparticle characterization", *Journal of the Optical Society of America. A*, Vol. 24, No. 9, pp. 2578–2589, 2007.

39. Charnigo, R., M. Francoeur, P. Kenkel, M. Pinar Mengüç, B. Hall and C. Srinivasan, "Estimating quantitative features of nanoparticles using multiple derivatives of scattering profiles", *Journal of Quantitative Spectroscopy and Radiative Transfer*, Vol. 112, No. 8, pp. 1369–1382, 2011.

40. Burr, D. W., K. J. Daun, O. Link, K. A. Thomson and G. J. Smallwood, "Determi-

nation of the soot aggregate size distribution from elastic light scattering through Bayesian inference", *Journal of Quantitative Spectroscopy and Radiative Transfer*, Vol. 112, No. 6, pp. 1099–1107, 2011.

41. Sipkens, T. A., R. Mansmann, K. J. Daun, N. Petermann, J. T. Titantah, M. Karttunen, H. Wiggers, T. Dreier and C. Schulz, "In situ nanoparticle size measurements of gas-borne silicon nanoparticles by time-resolved laser-induced incandescence", *Applied Physics B: Lasers and Optics*, Vol. 116, No. 3, pp. 623–636, 2014.

42. Otero, F. A., H. R. Barreto Orlande, G. L. Frontini and G. E. Eliçabe, "Bayesian approach to the inverse problem in a light scattering application", *Journal of Applied Statistics*, Vol. 42, No. 5, pp. 994–1016, 2015.

43. Clementi, L. A., J. R. Vega, L. M. Gugliotta and H. R. Orlande, "A Bayesian inversion method for estimating the particle size distribution of latexes from multiangle dynamic light scattering measurements", *Chemometrics and Intelligent Laboratory Systems*, Vol. 107, No. 1, pp. 165–173, 2011.

44. Charnigo, R., M. Francoeur, P. Kenkel, M. P. Menguc, B. Hall and C. Srinivasan, "Credible intervals for nanoparticle characteristics", *Journal of Quantitative Spectroscopy and Radiative Transfer*, Vol. 113, No. 2, pp. 182–193, 2012.

45. Hadwin, P. J., T. A. Sipkens, K. A. Thomson, F. Liu and K. J. Daun, "Quantifying uncertainty in soot volume fraction estimates using Bayesian inference of auto-correlated laser-induced incandescence measurements", *Applied Physics B*, Vol. 122, No. 1, pp. 1–16, 2016.

46. Ericok, O. B. and H. Erturk, "Characterization of nanoparticle aggregates using Bayesian inference via light scattering experiments", *ASME International Mechanical Engineering Congress and Exposition*, Phoenix, 2016.

47. Leuenberger, C. and D. Wegmann, "Bayesian computation and model selection without likelihoods", *Genetics*, Vol. 184, No. 1, pp. 243–252, 2010.

48. Tanaka, M. M., A. R. Francis, F. Luciani and S. A. Sisson, "Using approximate bayesian computation to estimate tuberculosis transmission parameters from genotype data", *Genetics*, Vol. 173, No. 3, pp. 1511–1520, 2006.

49. Weyant, A., C. Schafer and W. M. Wood-Vasey, "Likelihood-free cosmological inference with type Ia supernovae: approximate bayesian computation for a complete treatment of uncertainty", *The Astrophysical Journal*, Vol. 764, No. 2, pp. 116–130, 2013.

50. Turner, B. M. and T. Van Zandt, "Hierarchical Approximate Bayesian Computation", *Psychometrika*, Vol. 1, No. 2, pp. 185–209, 2014.

51. Jackson, J. D., *Classical Electrodynamics*, Wiley, New York, 3rd edn., 1999.

52. Bohren, C. E. and D. R. H. Wiley, *Absorption and Scattering of Light by Small Particles*, John Wiley & Sons, 1984.

53. Filippov, A., M. Zurita and D. Rosner, "Fractal-like aggregates: Relation between morphology and physical properties", *Journal of Colloid and Interface Science*, Vol. 229, No. 1, pp. 261–273, 2000.

54. Skorupski, K., J. Mroczka, T. Wriedt and N. Riefler, "A fast and accurate implementation of tunable algorithms used for generation of fractal-like aggregate models", *Physica A: Statistical Mechanics and its Applications*, Vol. 404, pp. 106–117, 2014.

55. Marsaglia, G., "Choosing a Point from the Surface of a Sphere", *The Annals of Mathematical Statistics*, Vol. 43, No. 2, pp. 645–646, 1972.

56. Ma, L., "Analysis of error in soot characterization using scattering-based techniques", *Particuology*, Vol. 9, No. 3, pp. 210–214, 2011.

57. Yon, J., F. Liu, A. Bescond, C. Caumont-Prim, C. Rozé, F. X. Ouf and A. Coppalle,

"Effects of multiple scattering on radiative properties of soot fractal aggregates", *Journal of Quantitative Spectroscopy and Radiative Transfer*, Vol. 133, pp. 374–381, 2014.

58. Bond, T. C. and R. W. Bergstrom, "Light Absorption by Carbonaceous Particles: An Investigative Review", *Aerosol Science and Technology*, Vol. 40, No. 1, pp. 27–67, 2006.

59. Yon, J., R. Lemaire, E. Therssen, P. Desgroux, a. Coppalle and K. F. Ren, "Examination of wavelength dependent soot optical properties of diesel and diesel/rapeseed methyl ester mixture by extinction spectra analysis and LII measurements", *Applied Physics B: Lasers and Optics*, Vol. 104, No. 2, pp. 253–271, 2011.

60. Prasanna, S., P. Rivière and A. Soufiani, "Effect of fractal parameters on absorption properties of soot in the infrared region", *Journal of Quantitative Spectroscopy and Radiative Transfer*, Vol. 148, pp. 141–155, 2014.

61. Sorensen, C. M. and W. B. Hageman, "Two-dimensional soot", *Langmuir*, Vol. 17, No. 18, pp. 5431–5434, 2001.

62. Dobbins, R. a., "Hydrocarbon nanoparticles formed in flames and diesel engines", *Aerosol Science and Technology*, Vol. 41, No. 5, pp. 485–496, 2007.

63. Wu, Y., T. Cheng, L. Zheng and H. Chen, "Effect of morphology on the optical properties of soot aggregated with spheroidal monomers", *Journal of Quantitative Spectroscopy and Radiative Transfer*, Vol. 168, pp. 158–169, 2016.

64. Tian, K., F. Liu, K. A. Thomson, D. R. Snelling, G. J. Smallwood and D. Wang, "Distribution of the number of primary particles of soot aggregates in a non-premixed laminar flame", *Combustion and Flame*, Vol. 138, No. 1-2, pp. 195–198, 2004.

65. Yurkin, M. A. and A. G. Hoekstra, "The discrete dipole approximation: An

overview and recent developments", *Journal of Quantitative Spectroscopy and Radiative Transfer*, Vol. 106, No. 1-3, pp. 558–589, 2007.

66. Hull, P., I. Shepherd and A. Hunt, "Modeling light scattering from Diesel soot particles", *Applied Optics*, Vol. 43, No. 17, pp. 3433–3441, 2004.

67. Berg, M. J. and C. M. Sorensen, "Internal fields of soot fractal aggregates", *J Opt Soc Am A Opt Image Sci Vis*, Vol. 30, No. 10, pp. 1947–1955, 2013.

68. Liu, F. and G. J. Smallwood, "Radiative Properties of Numerically Generated Fractal Soot Aggregates: The Importance of Configuration Averaging", *Journal of Heat Transfer*, Vol. 132, No. 2, pp. 023308–1–023308–6, 2010.

69. Instruments, H., *Technology for Polarization Measurement Exicor 150XT*, Tech. rep., 2013.

70. Ericok, O. B. and H. Ertürk, "Inverse characterization of nanoparticle clusters using unpolarized optical scattering without ex-situ measurements", *Journal of Quantitative Spectroscopy and Radiative Transfer*, Vol. 198, pp. 117–129, 2017.

71. Baneshi, M., S. Maruyama and A. Komiya, "Infrared Radiative Properties of Thin Polyethylene Coating Pigmented With Titanium Dioxide Particles", *Journal of Heat Transfer*, Vol. 132, No. 2, pp. 023306–023306, 2010.

72. Alifanov, O. M., *Inverse Heat Transfer Problems*, Springer-Verlag, Berlin, 1994.

73. Ozisik, M. N. and H. R. Orlande, *Inverse Heat Transfer*, Taylor & Francis, New York, 2000.

74. Glover, F., "Tabu Search - Part I", *ORSA journal on Computing*, Vol. 1, No. 3, pp. 190–206, 1989.

75. Siarry, P. and G. Berthiau, "Fitting of Tabu Search To Optimize Functions of Continuous Variables", *International Journal for Numerical Methods in Engineering*,

Vol. 40, No. 13, pp. 2449–2457, 1997.

76. Chelouah, R. and P. Siarry, "Tabu search applied to global optimization", *European Journal of Operational Research*, Vol. 123, No. 2, pp. 256–270, 2000.

77. Ayranci, I., R. Vaillon and N. Selçuk, "Performance of discrete dipole approximation for prediction of amplitude and phase of electromagnetic scattering by particles", *Journal of Quantitative Spectroscopy and Radiative Transfer*, Vol. 103, No. 1, pp. 83–101, 2007.

78. Yon, J., C. Rozé, T. Girasole, A. Coppalle and L. Méès, "Extension of RDG-FA for scattering prediction of aggregates of soot taking into account interactions of large monomers", *Particle and Particle Systems Characterization*, Vol. 25, No. 1, pp. 54–67, 2008.

79. Loke, V. L. Y., G. M. Huda, E. U. Donev, V. Schmidt, J. T. Hastings, M. P. Mengüç and T. Wriedt, "Comparison between discrete dipole approximation and other modelling methods for the plasmonic response of gold nanospheres", *Applied Physics B: Lasers and Optics*, Vol. 115, No. 2, pp. 237–246, 2014.

80. Xu, C., X. Cai, J. Zhang and L. Liu, "Fast nanoparticle sizing by image dynamic light scattering", *Particuology*, Vol. 19, pp. 82–85, 2014.

81. Bertsekas, D. P. and J. N. Tsitsiklis, *Introduction to Probability*, Athena Scientific, Belmont, Massachusetts, 2 edn., 2008.

82. Kaipio, J., E. Somersalo, E. S. S. Antman, J. E. M. L. Sirovich, A. J. K. Hale, P. H. J. Keener, J. K. B. J. Matkowsky and A. M. C. S. Peskin, *Statistical and Computational Inverse Problems*, Vol. 160, Springer, New York, kaipio2004 edn., 2004.

83. Tavaré, S., D. J. Balding, R. C. Griffiths and P. Donnelly, "Inferring coalescence times from DNA sequence data", *Genetics*, Vol. 145, No. 2, pp. 505–518, 1997.

84. Pritchard, J. K., M. T. Seielstad, A. P-L and M. W. Feldman, "Population growth of human Y chromosomes: a study of Y chromosome microsatellites", *Mol Biol Evol*, Vol. 16, pp. 1791–1798, 1999.

85. Marjoram, P., J. Molitor, V. Plagnol and S. Tavare, "Markov chain Monte Carlo without likelihoods.", *Proceedings of the National Academy of Sciences of the United States of America*, Vol. 100, No. 26, pp. 15324–15328, 2003.

86. Gelman, A., J. B. Carlin, H. S. Stern, D. B. Dunson, A. Vehtari and D. B. Rubin, *Bayesian Data Analysis*, CRC Press, 3 edn., 2014.

87. Robert, C. and G. Casella, *Monte Carlo Statistical Methods*, Springer, 2004.

88. Turner, B. M. and T. Van Zandt, "A tutorial on approximate Bayesian computation", *Journal of Mathematical Psychology*, Vol. 56, No. 2, pp. 69–85, 2012.

89. Sisson, S. A., Y. Fan and M. M. Tanaka, "Sequential Monte Carlo without likelihoods", *Proceedings of the National Academy of Sciences of the United States of America*, Vol. 104, No. 6, pp. 1760–1765, 2007.

90. Beaumont, M. A., J. Cornuet, J. Marin and C. P. Robert, "Adaptive approximate Bayesian computation", *Biometrika*, Vol. 96, No. 4, pp. 983–990, 2009.

91. Wegmann, D., C. Leuenberger, S. Neuenschwander and L. Excoffier, "ABCtoolbox: a versatile toolkit for approximate Bayesian computations.", *BMC bioinformatics*, Vol. 11, 2010.

92. Drovandi, C. C. and A. N. Pettitt, "Estimation of Parameters for Macroparasite Population Evolution Using Approximate Bayesian Computation", *Biometrics*, Vol. 67, No. 1, pp. 225–233, 2011.

93. Del Moral, P., A. Doucet and A. Jasra, "An adaptive sequential Monte Carlo method for approximate Bayesian computation", *Statistics and Computing*,

Vol. 22, No. 5, pp. 1009–1020, 2012.

94. Lenormand, M., F. Jabot and G. Deffuant, "Adaptive approximate Bayesian computation for complex models", *Computational Statistics*, Vol. 28, No. 6, pp. 2777–2796, 2013.

95. Liu, F., B. J. Stagg, D. R. Snelling and G. J. Smallwood, "Effects of primary soot particle size distribution on the temperature of soot particles heated by a nanosecond pulsed laser in an atmospheric laminar diffusion flame", *International Journal of Heat and Mass Transfer*, Vol. 49, No. 3-4, pp. 777–788, 2006.

96. Hamilton, W. R., "On quaternions; or on a new system of imaginaries in algebra", *Philosophical Magazine Series 3*, Vol. 25, pp. 10–13, 1844.

97. Hamilton, W. R., *Lectures on Quaternions: containing a systematic statement of a new mathematical method*, Dublin: Hodges and Smith, 1853.

98. Altmann, S. L., *Rotations, Quaternions, and Double Groups*, Oxford University Press, New York, 1986.

APPENDIX A: QUATERNION ROTATION

As mentioned in the Chapter 3, the Filippov's algorithm necessitates rotation of vectors about other vectors. This can be a very challenging task that can lead many errors unless quaternion rotation operator is used. In this section, the rotation of vectors using quaternions will be explained gradually by introducing fundametal quaternion algebra first. After all the necessary algebra is introduced the rotation theorem using quaternions will be introduced and proved mathematically.

A.1. Basic Algebraic Operations

In this section, the basic algebraic operations with quaternions will be introduced. Introduction of these algebraic operations is essential to understand the quaternions and they will be used to prove the rotation theorem.

The quaternions are introduced by W. R. Hamilton [96]. It is rumoured that he suddenly got the idea when he was walking with his wife Helen on their way to Royal Irish Academy. At that moment, he carved the equations into the stone of Brougham Bridge.

$$\hat{\mathbf{i}}^2 = \hat{\mathbf{j}}^2 = \hat{\mathbf{k}}^2 = \hat{\mathbf{i}}\hat{\mathbf{j}}\hat{\mathbf{k}} = -1$$

Using the rules introduced by Hamilton, quaternions can be defined as

$$q = q_0 + q_1\hat{\mathbf{i}} + q_2\hat{\mathbf{j}} + q_3\hat{\mathbf{k}} = q_0 + \mathbf{q} \tag{A.1}$$

where $\mathbf{q}$ is a vector in 3 dimensional space with $\mathbf{q} = (q_1, q_2, q_3)$. Notice that the vector notation is adopted to represent the quaternions in a more compact way. This representation will be useful especially in long equations.

Operations of addition, multiplication, complex conjugate and norm are the only ones that will be reviewd here. Other algebraic operation such as inverse, exponential of a quaternion etc. can be found in elsewhere [97], [98].

A.1.1. Addition

Addition, the first fundamental algebraic operation, is performed component-wise for two quaternions p and q.

$$\begin{aligned} p + q &= (p_0 + q_0) + (p_1 + q_1)\hat{\mathbf{i}} + (p_2 + q_2)\hat{\mathbf{j}} + (p_3 + q_3)\hat{\mathbf{k}} \\ &= (p_0 + q_0) + (\mathbf{p} + \mathbf{q}) \end{aligned}$$

In the case of subtraction, addition rule with the negative of a quaternion should be used. Negative of a quaternion is defined as the negative of each component, $-q = -q_0 - \mathbf{q}$.

A.1.2. Multiplication

Following the rules introduced by Hamilton, multiplication operation is defined as

$$\begin{aligned} pq &= (p_0 + p_1\hat{\mathbf{i}} + p_2\hat{\mathbf{j}} + p_3\hat{\mathbf{k}})(q_0 + q_1\hat{\mathbf{i}} + q_2\hat{\mathbf{j}} + q_3\hat{\mathbf{k}}) \\ &= p_0q_0 - (p_1q_1 + p_2q_2 + p_3q_3) + p_0(q_1\hat{\mathbf{i}} + q_2\hat{\mathbf{j}} + q_3\hat{\mathbf{k}}) + q_0(p_1\hat{\mathbf{i}} + p_2\hat{\mathbf{j}} + p_3\hat{\mathbf{k}}) \\ &\quad + \hat{\mathbf{i}}(p_2q_3 - p_3q_2) + \hat{\mathbf{j}}(p_3q_1 - p_1q_3) + \hat{\mathbf{k}}(p_1q_2 - p_2q_1) \\ &= p_0q_0 - \mathbf{p}\cdot\mathbf{q} + p_0\mathbf{q} + q_0\mathbf{p} + \mathbf{p}\times\mathbf{q} \end{aligned}$$

Again, the vector notation of quaternions simplify the resulting expression remarkably.

A.1.3. Complex Conjugate

Complex conjugate of quaternion is similar to complex conjugate of complex numbers.

$$\begin{aligned} q^* &= q_0 - q_1\hat{\mathbf{i}} - q_2\hat{\mathbf{j}} - q_3\hat{\mathbf{k}} \\ &= q_0 - \mathbf{q} \end{aligned}$$

Some useful relations such as $(q^*)^* = q$, $q + q^* = 2q_0$, $qq^* = q^*q$ and $(pq)^* = q^*p^*$ can be derived easily.

A.1.4. Norm

With the definiton of the complex conjugate operation the norm of a quaternion can be defined as

$$\begin{aligned} |q| &= \sqrt{q^*q} \\ &= \sqrt{q_0^2 + q_1^2 + q_2^2 + q_3^2} \end{aligned}$$

A quaternion is called as *unit quaternion* if its norm is 1. Moreover, the norm of the product of two quaternions is the product of the norm of each quaternion.

$$\begin{aligned} |pq| &= \sqrt{(pq)^*(pq)} \\ &= \sqrt{q^*p^*pq} \\ &= \sqrt{p^*pq^*q} \\ &= \sqrt{|p|^2|q|^2} \\ &= |p||q| \end{aligned}$$

A.2. The Rotation Operator

Quaternions can simply be viewed as vectors in 4 dimension. Then, the first question is how they can operate on vectors in 3 dimensional space. The answer to this question is hidden in the definiton of a quaternion. A 3 dimensional vector as we know it is actually a quaternion with 0 real part! This special type of quaternions are called as *pure quaternions*.

The operator L that operates on vectors $\mathbf{v} \in \Re^3$ is defined in the following form

$$L(\mathbf{v}) = q\mathbf{v}q^* = \left(q_0^2 - |\mathbf{q}|^2\right)\mathbf{v} + 2(\mathbf{q}\cdot\mathbf{v})\,\mathbf{q} + 2q_0(\mathbf{q}\times\mathbf{v}) \tag{A.2}$$

where q is the unit quaternion.

The proposed operator has three vital features. First one is that the length of the resulting vector, $L(\mathbf{v})$, remains unchanged.

$$\begin{aligned} |L(\mathbf{v})| &= |q\mathbf{v}q^*| \\ &= |q||\mathbf{v}||q^*| \\ &= |\mathbf{v}| \end{aligned}$$

Second feature is that the direction of the vector $\mathbf{v}$ remains unchanged if the vector $\mathbf{v}$ is along the vector $\mathbf{q}$. In other words, if we can represent $\mathbf{v} = k\mathbf{q}$, action of L on $\mathbf{v}$ is

$$
\begin{aligned}
L(\mathbf{v}) &= q\mathbf{v}q^* \\
&= q(k\mathbf{q})q^* \\
&= \left(q_0^2 - |\mathbf{q}|^2\right)(k\mathbf{q}) + 2(\mathbf{q}\cdot(k\mathbf{q}))\mathbf{q} + 2q_0(\mathbf{q}\times(k\mathbf{q})) \\
&= \left(q_0^2 - |\mathbf{q}|^2\right)(k\mathbf{q}) + 2|\mathbf{q}|^2(k\mathbf{q}) \\
&= \left(q_0^2 + |\mathbf{q}|^2\right)(k\mathbf{q}) \\
&= (k\mathbf{q}) \\
&= \mathbf{v}
\end{aligned}
$$

where the simplifications are due to $|q| = 1$ and $\mathbf{q}\times\mathbf{q} = 0$. It can be observed that the resulting vector $L(\mathbf{v})$ is exactly same as the input $\mathbf{v}$. Note that obtaining the same vector at the end is a special case since the vector $\mathbf{v}$ is in the direction of $\mathbf{q}$. This observation is essential for the quaternion rotation theorem.

Lastly, the operator L is linear over $\Re^3$, meaning that for any two vectors $\mathbf{v}_1$ and $\mathbf{v}_2$ we will have

$$L(c_1\mathbf{v}_1 + c_2\mathbf{v}_1) = c_1L(\mathbf{v}_1) + c_2L(\mathbf{v}_2)$$

where the coefficients $c_1, c_2 \in \Re$.

Theorem A.1. *The operator L rotates the vector $\mathbf{v}$ about the axis $\hat{\mathbf{e}}$ by an angle θ*

$$L(\mathbf{v}) = q\mathbf{v}q^*$$

where q is unit quaternion with $q = q_0 + \mathbf{q} = \cos\frac{\theta}{2} + \hat{\mathbf{e}}\sin\frac{\theta}{2}$ and $\hat{\mathbf{e}}$ is the unit vector along $\mathbf{q}$.

Proof. The vector $\mathbf{v}$ can be decomposed into its components as $\mathbf{v} = \mathbf{v}_\parallel + \mathbf{v}_\perp$ where $\mathbf{v}_\parallel$ and $\mathbf{v}_\perp$ are the components of $\mathbf{v}$ along and normal to $\mathbf{q}$, respectively. We have

previously shown that $\mathbf{v}_{\parallel}$ is invariant under operator L. Therefore, we only need to show that the resulting vector after operator L is performed on the perpendicular component of $\mathbf{v}$ is indeed the rotation of vector $\mathbf{v}$ about the axis $\mathbf{q}$ by an angle θ. If we operate L on $\mathbf{v}_{\perp}$

$$\begin{aligned} L(\mathbf{v}_{\perp}) &= \left(q_0^2 - |\mathbf{q}|^2\right)\mathbf{v}_{\perp} + 2(\mathbf{q}\cdot\mathbf{v}_{\perp})\,\mathbf{q} + 2q_0(\mathbf{q}\times\mathbf{v}_{\perp}) \\ &= \left(q_0^2 - |\mathbf{q}|^2\right)\mathbf{v}_{\perp} + 2q_0(\mathbf{q}\times\mathbf{v}_{\perp}) \\ &= \left(q_0^2 - |\mathbf{q}|^2\right)\mathbf{v}_{\perp} + 2q_0|\mathbf{q}|(\hat{\mathbf{e}}\times\mathbf{v}_{\perp}) \end{aligned}$$

Note that second term of the first equation vanishes due to the orthogonality of $\mathbf{q}$ and $\mathbf{v}_{\perp}$. Moreover, the vector $\mathbf{q}$ in the last step is substituted by $\mathbf{q} = |\mathbf{q}|\hat{\mathbf{e}}$ since $\hat{\mathbf{e}}$ is the unit vector along the direction of $\mathbf{q}$. If we introduce $\mathbf{n}$ as $\mathbf{n} = \hat{\mathbf{e}}\times\mathbf{v}_{\perp}$ a new coordinate system shown in Figure A.1 will be introduced.

$$L(\mathbf{v}_{\perp}) = \left(q_0^2 - |\mathbf{q}|^2\right)\mathbf{v}_{\perp} + 2q_0|\mathbf{q}|\mathbf{n} \tag{A.3}$$

Notice that the length of $\mathbf{n}$ is equal to that of $\mathbf{v}_{\perp}$ since $|\hat{\mathbf{e}}| = 1$.

$$|\mathbf{n}| = |\hat{\mathbf{e}}\times\mathbf{v}_{\perp}| = 1\cdot|\mathbf{v}_{\perp}|\sin\frac{\theta}{2} = |\mathbf{v}_{\perp}|$$

Substituting necessary values into Equation A.3 results into the final form

$$\begin{aligned} L(\mathbf{v}_{\perp}) &= \left(\cos^2\frac{\theta}{2} - \sin^2\frac{\theta}{2}\right)\mathbf{v}_{\perp} + \left(2\cos\frac{\theta}{2}\sin\frac{\theta}{2}\right)\mathbf{n} \\ &= \cos\theta\mathbf{v}_{\perp} + \sin\theta\mathbf{n} \end{aligned}$$

Figure A.1 shows the new coordinate system described by the equation $\mathbf{n}$ as $\mathbf{n} = \hat{\mathbf{e}}\times\mathbf{v}_{\perp}$. Observe that the resulting expression, $L(\mathbf{v}_{\perp})$, is indeed the rotation of $\mathbf{v}_{\perp}$ about unit vector $\hat{\mathbf{e}}$ by an angle θ. □

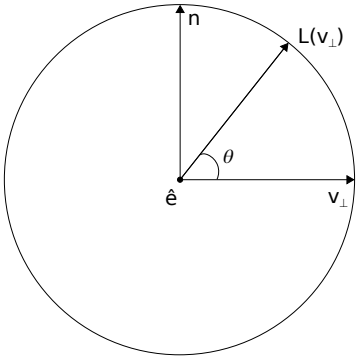

Figure A.1. The resulting vector when the rotation operator L is applied to $\mathbf{v}_\perp$.